

AD_____

Award Number: W81XWH-11-2-0187

TITLE: Neuroperformance Imaging

PRINCIPAL INVESTIGATOR: Seong K. Mun, PhD

CONTRACTING ORGANIZATION: VIRGINIA POLYTECHNIC INSTITUTE & STATE U
Blacksburg, VA 24060-3580

REPORT DATE: October 2012

TYPE OF REPORT: Annual

PREPARED FOR: U.S. Army Medical Research and Materiel Command
Fort Detrick, Maryland 21702-5012

DISTRIBUTION STATEMENT: Approved for Public Release;
Distribution Unlimited

The views, opinions and/or findings contained in this report are those of the author(s) and should not be construed as an official Department of the Army position, policy or decision unless so designated by other documentation.

REPORT DOCUMENTATION PAGE			<i>Form Approved</i> <i>OMB No. 0704-0188</i>		
Public reporting burden for this collection of information is estimated to average 1 hour per response, including the time for reviewing instructions, searching existing data sources, gathering and maintaining the data needed, and completing and reviewing this collection of information. Send comments regarding this burden estimate or any other aspect of this collection of information, including suggestions for reducing this burden to Department of Defense, Washington Headquarters Services, Directorate for Information Operations and Reports (0704-0188), 1215 Jefferson Davis Highway, Suite 1204, Arlington, VA 22202-4302. Respondents should be aware that notwithstanding any other provision of law, no person shall be subject to any penalty for failing to comply with a collection of information if it does not display a currently valid OMB control number. PLEASE DO NOT RETURN YOUR FORM TO THE ABOVE ADDRESS.					
1. REPORT DATE 19 October 2012		2. REPORT TYPE Annual		3. DATES COVERED 20 September 2011-19 September 2012	
4. TITLE AND SUBTITLE Neuroperformance Imaging			5a. CONTRACT NUMBER		
			5b. GRANT NUMBER W81XWH-11-2-0187		
			5c. PROGRAM ELEMENT NUMBER		
6. AUTHOR(S) Seong K. Mun,Linda Larson-Prior, Kenneth Wong, Alpay Ozcan E-Mail: munsk@vt.edu			5d. PROJECT NUMBER		
			5e. TASK NUMBER		
			5f. WORK UNIT NUMBER		
7. PERFORMING ORGANIZATION NAME(S) AND ADDRESS(ES) Virginia Tech, Office of Sponsored Programs Blacksburg, VA 24061			8. PERFORMING ORGANIZATION REPORT NUMBER		
9. SPONSORING / MONITORING AGENCY NAME(S) AND ADDRESS(ES) U.S. Army Medical Research and Materiel Command Fort Detrick, Maryland 21702-5012			10. SPONSOR/MONITOR'S ACRONYM(S)		
			11. SPONSOR/MONITOR'S REPORT NUMBER(S)		
12. DISTRIBUTION / AVAILABILITY STATEMENT Approved for Public Release; Distribution Unlimited					
13. SUPPLEMENTARY NOTES					
14. ABSTRACT - We have designed an appropriate PET imaging protocol that will allow us to differentiate regional metabolic activity between different sleep cycle periods. Pilot diffusion MRI data using phantoms has informed a new and more accurate mathematical model, CFD-MRI, for MR tractography. The analysis indicates the necessity of further investigations for better understanding and quantifying various artifacts in data collection. Using the simultaneous fMRI-EEG data techniques, brain regions of interest and their activity has been identified. The results of these studies clearly indicate changes in resting state brain network connectivity in the transition from alert wakefulness to sleep.					
15. SUBJECT TERMS Neuroperformance, Sleep cycle, metabolism, thalamic structures, PET Imaging, MR Imaging, functional MRI, electroencephalography (EEG)					
16. SECURITY CLASSIFICATION OF:			17. LIMITATION OF ABSTRACT	18. NUMBER OF PAGES	19a. NAME OF RESPONSIBLE PERSON
a. REPORT	b. ABSTRACT	c. THIS PAGE			USAMRMC
U	U	U	UU	47	19b. TELEPHONE NUMBER (include area code)

Table of Contents

Introduction	4
Body	4
Key Research Accomplishments	10
Reportable Outcomes	10
Conclusion	12
References	13
Appendices	14

Introduction

Sleep restriction and deprivation have profound negative effects on cognitive ability and task performance (e.g., vigilance). At the same time, physical and psychological stressors often lead to sleep disruptions, which compromise the body's ability to reap the restorative benefits of sleep. Military personnel often suffer from decreased **quality** and **quantity** of sleep, increasing their susceptibility to a host of neurological problems and limiting their ability to perform the challenging mental tasks that their missions require. Further, the effects of pharmacological interventions aimed at ameliorating the deleterious effects of both sleep loss and mental and physical stress are only poorly understood and may result in unanticipated long-term effects in those serving under combat conditions. Advances in imaging technology have enabled human studies of neurochemistry, energy metabolism and functional brain networks that were previously impossible.

Our research uses a combination of human imaging-based studies to advance our fundamental knowledge of the effects of sleep and sleep-related stressors on neuroperformance. In order to achieve this goal, the team utilizes ultra-high resolution imaging hardware, 7T MRI scanner and High Resolution PET (HRRT) scanner in tandem. These scanners at Neuroscience Research Institute at Gachon University are conveniently positioned so to be linked by a patient tray system, unique around the world, that can carry the subject from one scanner to the other, thereby keeping the reference frames of each modality intact and physically registered. The removal of software image registration from data analysis, as well as prevention of signal loss by the absence of physical/electrical interactions between the devices results in unprecedented high quality, ultra-high resolution images.

Adding this unique high precision setup to our capabilities, the scope of this research is to 1) use PET/MRI studies to understand glucose metabolism and dopamine binding in the brain, particularly in the brainstem and thalamus; 2) EEG/fMRI studies focusing on the functional connectivity of networks between the thalamus and cortex that control the descent into sleep and are altered by sleep deprivation; 3) EEG/fMRI studies designed to improve our understanding of the interaction between sleep loss, emotional stress and cognitive function, and 4) Development of reference image databases for high field MRI studies of the brain.

Body

The research accomplishments associated with each task outlined in the approved Statement of Work for year 1 are as follows:

A. PET/MRI studies of brainstem and cortex sleep regulation

A1. Provide sleep neuroscience expertise to the Neuroscience Research Institute (NRI) of Gachon University for PET/MRI studies.

A1.1. Initial training in the Neurobiology of Sleep and Sleep Medicine was provided by Dr. Larson-Prior beginning in November of 2010. Training included both didactic information and hands-on practical training in sensor application and quality control, reading of the acquired electroencephalographic (EEG) signal, and subject comfort. During this pre-award training period, preliminary studies provided important information to study design and implementation.

A1.2 *Workshop on Study of Neuro-Stress with MRI Tractography and PET Imaging*

To achieve an efficient transfer of expertise with a wide foundation, we organized an International Workshop, titled **Study of Neuro-Stress with MRI Tractography and PET Imaging** at Neuroscience Research Institute, Gacheon University, Incheon, Korea Feb 16-17, 2011. Invited speakers were specifically chosen from United States and Korea to facilitate the exchange of ideas between the researchers. The workshop included presentations from different disciplines, PET-MR fusion for neuroimaging, animal models of traumatic injuries, fundamentals of diffusion imaging, application of multi-modality imaging in sleep studies and an introduction to prospects of connectomics (see Appendix 1 for the participant and talk lists). Presented below is the workshop announcement:

Recent advances in diffusion weighted (DW) magnetic resonance imaging (MRI) provided non-invasive, in vivo means for assessment of white matter integrity in human subjects. The state of the art instrumentation based on 7T MRI, high resolution PET imaging and novel mathematical approaches of data analysis and visualization made it possible to envision the use of DWI to study white matter integrity along with nerve fiber connections.

Consequently, recent studies of several diseases and disorders unveiled accurate information about nerve fiber pathways and white matter integrity using DW-MRI. This provided improved guidance for diagnosis, prognosis and treatment of acute and chronic symptoms in neurological diseases and psychiatric disorders such as stroke, multiple sclerosis, epilepsy, Alzheimer's disease, Parkinson's disease, schizophrenia and depression and traumatic brain injury (TBI).

In addition to these disorders, the common and significant problem of stress itself has been associated with a number of physiological and psychological problems including, but not limited to, anxiety, depression, chronic sleep loss/insomnia, hypertension, migraine and other forms of headache, and poor decision making (executive functioning). The response to acute stress is likely to affect functional brain connectivity without producing significant changes in anatomical connectivity. However, the effects of chronic stress (continuous over more than 1 year as encountered by warfighters) are unknown. For warfighters both on active duty and home after having served under these conditions, there is ample evidence of chronic stress responses that are not alleviated simply by removing the individual from the field.

The successful developments of diffusion weighted neuroimaging raise the possibility of expanding the horizons of DW-MRI towards an assessment of stress related effects with the aim of enabling stress resistance. This workshop will discuss the potential of macro-connectomics inferred from tractography methods as an aid for the identification of those individuals at greatest risk for deleterious outcomes, for the development of effective treatment strategies and in the evaluation of the efficacy of interventions. Additional discussion will focus on the importance of multi-modal neuroimaging and functional imaging in determining the interactions between anatomical connectivity and pathologies, including the role of high resolution MRI, functional MRI (fMRI), high resolution molecular imaging using HRRT (High Resolution Research Tomography), positron emission tomography (PET) and electroencephalography (EEG).

This workshop is planned at the Neuroscience Research Institute of Gacheon University, Incheon, Korea, home of state of art neuroimaging instruments including 7T human MRI, High Resolution PET(HRRT), 3T MRI and ZOOM PET. The institute maintains its cutting edge status with a new project for the development of a 14T MRI system.

Workshop Feedback: Plenary speaker LG. (ret). James Peake indicated after praising the content of the workshop that the knowledge that will be obtained will outreach beyond the scope of sleep studies and will help us better understand and remedy the PTSD-TBI continuum which will affect a large population of returning warfighters. COL. Karl Friedl emphasized the importance of this opportunity which allows the convergence of different fields, medicine, neuroscience, physics and engineering in order to achieve breakthrough developments that will address not only battle field originating injuries such as TBI and PTSD but also accelerated neurodegenerative diseases, e.g. Alzheimer's disease, that is expected to affect a large portion of the aging population in the near future.

The workshop included presentations from different disciplines, PET-MR fusion for neuroimaging, animal models of traumatic injuries, fundamentals of diffusion imaging, application of multi-modality imaging in sleep studies and an introduction to prospects of connectomics (please refer to the program in the Appendix 1 for the participant and talk lists).

A2. Analysis of pre-existing, de-identified PET/MRI data.

A2.1. We are currently working with the IRB to obtain approval for use of existing data archives at Gachon University. In the meantime, we have modeled and designed an optimal protocol for future PET data studies

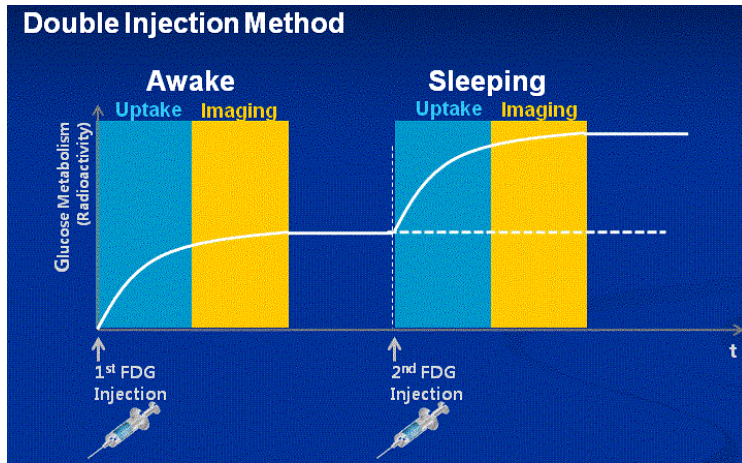


Figure 1. The initial study design called for two injections under the assumption that the radioactive decay curve would remain constant between injection periods. This allowed subtraction of residual radioactivity from the first injection to determine the correct values for responses to the second injection.

that will be provided by Gachon team. Our initial study design provided for injection of FDG at two points during the experimental period of overnight sleep (Figure 1). The implementation of this design required that the second injection occur at an asymptotic point on the FDG uptake curve while at the same time providing for only minor loss of radioactivity in our injection sample by the second time point. To achieve this 2-4 hours between injections (Figure 2A) needed to be allowed. Preliminary analysis of dual injections suggested that our assumption of an asymptotic concentration in residual radioactivity following the first inject was not being met (Figure 2B). To further test for decay dynamics, we implemented a dynamic scan protocol, which verified that levels were not consistent and precluded an accurate assessment of metabolic activity the initial experimental design (Figure 2). We then devised a protocol that allowed only a single FDG injection per study (Figure 3). This protocol required that only one sleep stage (either slow wave sleep [SWS] or rapid eye movement sleep [REM]) could be investigated in any individual subject during any one experimental night. As our protocol required one night of acclimatization sleep, these data were used to make a preliminary decision as to whether the Gachon team would provide data in REM or SWS in that subject.

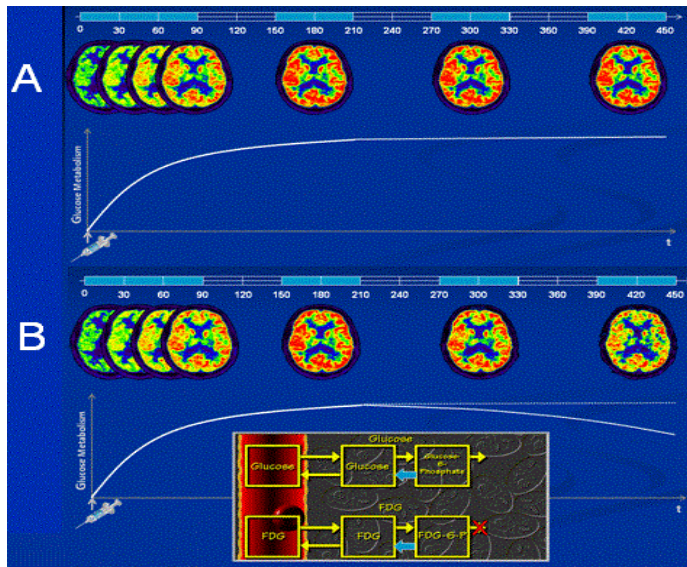


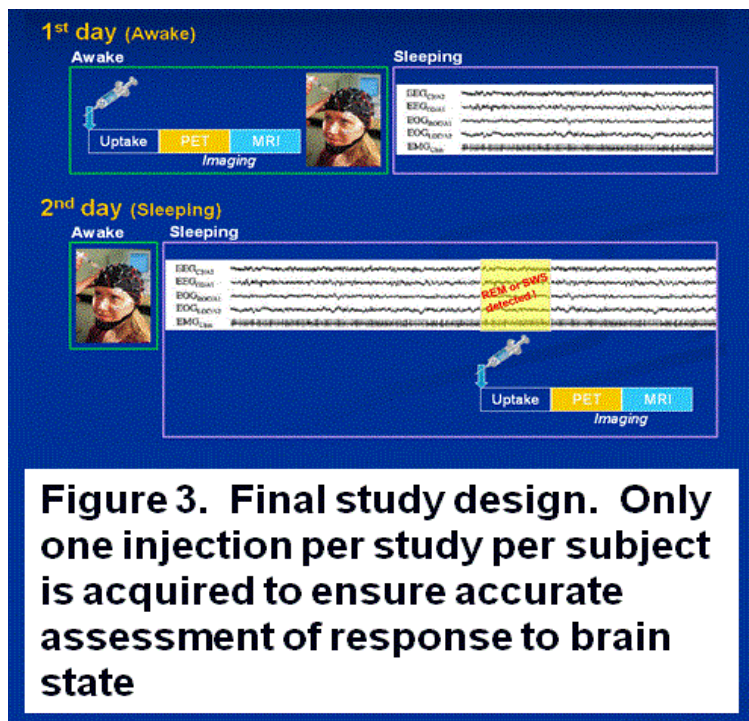
Figure 2. The assumed response required for accurate calculation of the response to second injection is shown in A. In B was the true response, indicating that we were not recovering an accurate response to the second injection

This was necessary as we required 30 minutes of in-stage uptake of our radio-nucleotide at different times during a normal night of sleep (SWS periods are longest early in the night while REM periods are longest late in the night). Gachon team successfully tested this protocol and are confident that they can use it for the planned studies.

As planning for the proposed PET and MRI studies, Gachon team also examined typical sleep patterns in potential volunteers. Questions were asked about the number of hours/night they slept, their normal bedtimes and wake times, and an overall score for sleep quality based on the Korean version of the Pittsburgh Sleep Quality Index (PSQI). The Epworth Sleepiness Scale provided information on daytime sleepiness in general, while the Stanford Sleep Index was used to assess each subject's level of sleepiness at a particular.

For the entire study group, subjects slept an average of 6.9 ± 1.0 hours per night. Most subjects reported no sleep disturbances (PSQI = 5.2 ± 1.8 ; normal sleep reports PSQI <10), although one subject reported mild sleep disturbance with a PSQI of 10 (a PSQI of >21 is considered

abnormal). The range of reported normal bedtimes was 11PM – 4AM, with most subjects reporting normal bedtimes around 2AM. Although this investigation was not part of the statement of work and therefore



cat or rodent models indicate that the midline raphe nuclei are highly active in wake, show reduced activity in NREM sleep states and are turned off in REM sleep. This would lead us to expect a reduction in FDG label as we moved from wake to SWS to REM.

A3. Collaborative development of new data processing and analysis methods.

A3.1. Diffusion MRI:

The new diffusion MRI method, Complete Fourier Direct MRI (CFD-MRI), developed by Dr. Ozcan provides an accurate way of measuring, quantifying and characterizing the motion of the molecules within the biological tissue. CFD-MRI is different than the existing methods by its simple presentation as a Fourier transform of the joint distribution function of the number of spins at a given location with given displacement integrals (1-3) (see also (4) in the Appendix 2 for a detailed description). The method does not rely on any assumptions on the stochastic properties (e.g. Markovian property) or structural properties (such as being symmetric) of the motion. This generality makes CFD-MRI a truly free model. Accordingly, the method provides better information about the microstructure of the tissue under investigation, leading to more accurate description of different types of pathologies, injuries and changes. A detailed comparison of the existing diffusion MR methods has been provided in our team's recent publication (5) (see the attached manuscript in Appendix 3). Mainly, CFD-MRI relies on the Hermitian symmetry of the diffusion weighted (DW) MR signal. The method's proof concept obtained using animal scanners and relatively simple (but time consuming) pulse gradient spin echo (PGSE) imaging protocol is being translated into 7T human scanners to use with the fast scanning methods. There are significant challenges that arise from the new method and 7T technology. First, the use of fast imaging techniques, namely echo planar imaging (EPI), creates distortions in the images. This effect is further enhanced specifically at 7T MR due to the high field. The correction methods introduced earlier by the Gachon team (6) is not applicable to CFD-MRI due to its specific high dimensional Fourier nature.

Furthermore, the novelty of CFD-MRI also brings demand for a significantly larger amount of sampling in the Fourier space using as well unusual time parameters compared to conventional diffusion imaging protocols. These required addressing technical difficulties originating from vendor specific definition of diffusion gradient vectors in pulse sequence programming. After our teams resolved these technical issues, Gachon team collected initial CFD data from a fixed human brain using the 7T scanner under the supervision of Dr. Ozcan. Considering the novelty of the mathematical model and the 7T hardware, specifically the artifacts created by the ultra-high magnetic field, the data are promising. However, there is a lot of room for improvement which will be achieved according the analysis of the data after mathematical modeling of the reasons behind the loss of Hermitian symmetry during data collection. We are

hypothesizing that whereas local loss of symmetry is due but not limited to susceptibility artifacts and magnetic field inhomogeneity, radio frequency (RF) pulse inhomogeneity might be causing the deviations. We will continue further our experiments with the inclusion of more fundamental steps as running them on liquid samples in order to identify the source of artifacts. In parallel, under the assumption that the deviation is not preventable with hardware/parameter adjustments in pulse programming, mathematical algorithms for phase correction towards the re-establishment of Hermitian symmetry are being developed.

Dr. Ozcan has shared the findings of CFD-MRI at NRI-UPenn Joint Mini Symposium, Neuroscience Research Institute, Gacheon University Incheon, Korea on Sept 27-28, 2012 and at the recent MICCAI 2012 Workshop on Computational Diffusion MRI, the 15th International Conference on Medical Image Computing and Computer Assisted Intervention, Nice, France.

Furthermore, with the aim of increasing collaborative efforts and gathering information from different research centers around the world, Dr. Ozcan is hosting a research topic for exploring different techniques including but not limited to diffusion MRI to explore white matter integrity. The research topic (article submission deadline was Oct. 15th 2012), which will appear on the open access *Frontiers in Physiology, Integrative Neuroscience*, has been specifically designed by Dr. Ozcan to better understand tractography's role in white matter integrity with the additional aim of uncovering the shortcomings of existing methods. The topic has attracted participation from different institutions, Harvard, Duke, Oregon Health Sciences, Vanderbilt Universities, Univ. of South Florida, Univ. of Wisconsin, Leiden University, The Netherlands and Aarhus University, Denmark. The description of the topic is the following:

http://www.frontiersin.org/Integrative_Neuroscience/researchtopics/New_Models_of_Diffusion_Weight/775
New Models of Diffusion Weighted MRI Signal and Alternative Methods for Characterization of White Matter Integrity

Recent advances in diffusion weighted (DW) magnetic resonance imaging (MRI) provided non-invasive, in vivo means for assessment of white matter integrity in human subjects. The novel mathematical approaches of data analysis and visualization made possible the use of DWI to study white matter integrity along with nerve fiber connections. Accordingly, recent tractography studies of several diseases and disorders unveiled information about nerve fiber pathways and white matter integrity. This has significantly improved guidance potential for diagnosis, prognosis and treatment of acute and chronic symptoms in neurological diseases and psychiatric disorders such as stroke, multiple sclerosis, epilepsy, Alzheimer's disease, Parkinson's disease, schizophrenia, depression and traumatic brain injury (TBI). A majority of tractography methods are based on diffusion tensor (DT) model which is limited in describing complex tissue structure such as the nerve fiber junctions. In addition, the constraints of higher order analysis methods, such as symmetry, prevent innately an elaborate description of biological tissue microstructure due to information loss/deterioration. These raise the concern about the sufficiency and the accuracy of white matter integrity/pathology information and metrics obtained with current methods. Consequently, after achieving the proof of utility, DW-MRI methodologies are currently open for improvements and refinements. The purpose of this special issue is to investigate new analysis methods and new mathematical models with possible introduction of new acquisition techniques. This will be achieved by returning to the first principles of DW-MRI signal formation in order to explore new horizons that remained veiled due to constraints and boundaries imposed by existing methodologies. Particular emphasis will be given to approaches that will allow unconstrained evidence based discoveries using DW-MRI signal. Biological, synthetic and numerical phantoms created for test and validation purposes are highly encouraged.

In parallel, physiological description of white matter integrity disruption and its reflection on DW-MRI signal is central to the theme of the special issue.

The aim is geared up towards the identification of the nerve fiber DW-MRI signal, separating the portion of the signal from other elements within biological tissue, whereby an accurate calculation of surrogate markers/descriptors of white matter integrity would be achieved. Accordingly, comparison and/or combination of alternative MRI methods (e.g. susceptibility imaging) with DW-MRI are in focus of interest and are highly welcomed.

The research topic is essential in understanding the changes in the white matter and MRI's limits to measure this changes including the cases where prolonged sleep deprivation leading to neurostress. By identifying the brain regions that are most affected, it would be possible to assess the level the warfighters are affected

during and after return from active duty. The topic's goal also includes the detection of traumatic brain injury (TBI) and its effects on brain tissue.

A4. Recruit new subjects for studies of normal sleep using FDG and raclopride.

Recruitment of new subjects is deferred until the completion of IRB approvals.

B. Studies of thalamo-cortical network function during sleep

B1. Analysis of pre-existing EEG/fMRI data on N1 and N2 sleep to determine changes in thalamo-cortical network connectivity in the descent to sleep.

B1.1 EEG/fMRI studies of sleep in normal human subjects.

Dr. Larson-Prior's laboratory developed the technique of simultaneous electroencephalography (EEG) and functional magnetic resonance imaging (fMRI) at Washington University in St. Louis, acquiring data from normal, neurologically healthy, young adult subjects during quiet waking rest (2005-2007) and in the descent to sleep (2007-2008). Data were acquired from a total of 67 right-handed individuals over this period, 57 of whom participated in studies designed to examine brain network activity during resting 30 subjects provided full and good quality data sets for analysis (7). Based upon analysis of EEG data, subjects were divided into three groups, 1) those who remained in an alert waking state during scanning (n=9), 2) those who were drowsy, failing into the transition state between wake and sleep (stage 1; n=16) and 3) those who were overtly asleep (stage 2, n=6).

Analysis of these data utilized the methods of blood oxygen level dependent (BOLD) functional connectivity to define a set of 151 functional brain regions of interest (7) which were then evaluated for each condition for correlated activity during the scan session. The results of these studies clearly indicate changes in resting state brain network connectivity in the transition from alert wakefulness to sleep. As anticipated, one change lay in the relationship between the default mode network (8), which is most active in non-task related rest signaling disengagement from the external world (9), and two networks involved in attending to and interacting with external stimuli (dorsal attention network, ATTN, (10); Executive control network EXEC, (11)). During quiet rest, the DMN is most active while the networks generally most active in response to environmental stimuli exhibit reduced activity (12); thus, these networks are anti-correlated in functional connectivity analyses. As individuals fall asleep, the strength of these anti-correlations was seen to be reduced (Figure 4) indicating a reduction in the strength of inter-network connectivity in the descent to sleep.

During quiet rest, there are strong correlations between mediodorsal thalamic regions and elements of the DMN (13). If these relationships are removed to enable an investigation of other brain regions associated with thalamic activity, one finds correlations to anterior cingulate, supplemental motor area, and the basal ganglia. Further, differences in mediodorsal thalamic connectivity differ between eyes closed and eyes open fixated conditions, with the fixation condition exhibiting positive correlations to the attentional networks (ATTN). During the descent to sleep, thalamic connectivity changes were primarily noted within the thalamus, with correlations strengthening between 5 thalamic regions from wake to stage 2 sleep (7).

B2. Data collection and analysis to (1) increase the number of subjects reaching N2 sleep, and (2) collect data from subjects reaching N3 sleep.

We will start data collection upon the completion of IRB approvals.

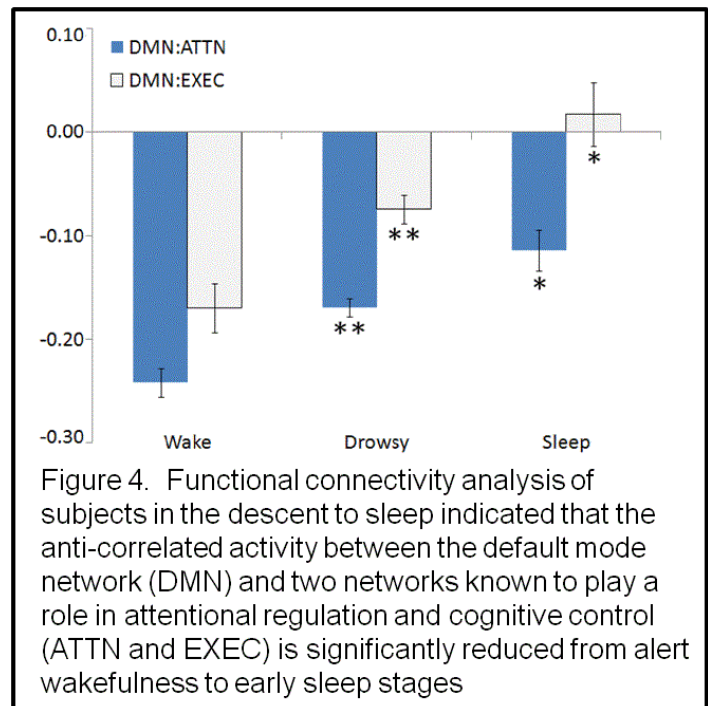


Figure 4. Functional connectivity analysis of subjects in the descent to sleep indicated that the anti-correlated activity between the default mode network (DMN) and two networks known to play a role in attentional regulation and cognitive control (ATTN and EXEC) is significantly reduced from alert wakefulness to early sleep stages

B3. Collect normative data on cognitive vigilance (PVT) prior to and following sleep (task flanks sleep) to analyze thalamo-cortical network interactions.

Normative data collection will be initiated upon the completion of IRB approvals.

C. Assemble and annotate a reference dataset of 7T brain images.

The 7T reference data set will be acquired after the completion of IRB approvals.

Preparations in Anticipation of Future Data Collection and Analysis

In order to address the variety of neuroscientific challenges that will be encountered with the data collection, Dr. Kathleen Gates, a neuroscientist, joined the Arlington Innovation Center in August 2012. Her work focuses on developing, testing, and applying novel methods that enable reliable inferences when studying individuals. In this vein, she has collaborated in research on mother-infant dyads, heart rate variability, and daily diary studies that attend to person-specific substantive questions. By the incorporation of Dr. Gates' expertise on developing statistical methods for analyzing brain imaging (7), the team's perspective and horizons has been prepared to tackle the complex challenges of neuroscience of sleep.

The IT infrastructure that will provide data storage, analysis using computational methods and facilitate communication between different centers of the project in a secure manner has been implemented at the Arlington Innovation Center. The network consists of a firewall and VPN device. Whereas publicly available information are presented at AIC webserver (Dell PowerEdge R310, 4 core Intel® Xeon® X3470, 16Gb memory, 4Tb raid 5 disk capacity), the collaborators in the project have the ability to access their data over a secure VPN connection on the computational server (Dell PowerEdge T710, 8 core Intel® Xeon® X5647, 96Gb memory, 14Tb raid 5 disk space) that is protected behind AIC firewall. The firewall and VPN services are provided by a Cisco ASA5520 appliance and Cisco 2960 switch. A beta version of in-house developed collaborative platform that allows the collaborators to drop and annotate data, manuscripts, presentations and documents have also been installed on the storage server. The platform will speed up data analysis and development of new ideas.

Key Research Accomplishments

- Provided initial training in the practical and theoretical basis of electroencephalography (EEG) for the study of human sleep to student researchers at the NRI, Gachon University
- In collaboration with colleagues at NRI, established a mechanism by which continued training in scoring sleep based on overnight EEG studies could be maintained
- All research team members worked to implement an optimal study design for initial investigations into brainstem regulation of human sleep using FDG-PET imaging
- IRB approval from Washington University in St. Louis was obtained for the prospective studies on cognition in sleep on 9/21/2012
- Programming of behavioral tasks is currently being done at Washington University in St. Louis preparatory to initiation of EEG/fMRI studies
- Further development of the new and more general method for diffusion weighted magnetic resonance imaging, Complete Fourier Direct MRI.

Reportable Outcomes

Manuscripts, abstracts, presentations:

- Dr. Larson-Prior provided didactic training in the Neurobiology of Sleep to students and faculty at the Neuroscience Research Institute at Gachon University in July 2011 with retroactive support from this grant. Presentation entitled: "Functional neural network modulation in wake, sleep and learning"
- In July 2011, Dr. Larson-Prior was asked to speak to MCB Korea on the importance of sleep in humans with retroactive support from this grant. This discussion was provided for the lay public and included a

short text that could be disseminated by MBC to the public. The presentation is included in the Appendix 4.

- Dr. Larson-Prior presented a summary of research progress and the rationale for the studies supported under this contract to Michael P. Brazaitis MD, MA, Program officer at TATRC entitled: “Sleep and Neuroperformance” in October 2011. At the same meeting Dr. Ozcan lead a discussion on the diffusion weighted imaging magnetic resonance imaging’s capabilities to detect white matter integrity using tractography in order to obtain a reference set for healthy population.
- Dr. Larson-Prior and Dr. Son presented their work, entitled “Brainstem Regulation of Sleep and Waking: A PET/MRI Perspective” at the Study of Neuro-Stress with MRI Tractography and PET Imaging Workshop, Neuroscience Research Institute, Gacheon University Incheon, Korea, Feb 16-17, 2012
- Larson-Prior, LJ, Power, JD, Vincent JL, Nlan, TS, Coalson, RS, Zempel, J, Snyder AZ, Schlaggar BL, Raichle, ME and Petersen SE (2011) [Modulation of the brain’s functional network architecture in the transition from wake to sleep](#). Prog Br Res, 193:277-294. PMID 21854969
- McAvoy, M, Larson-Prior, L, Ludwikow, M, Zhang, D, Snyder AZ, Gusnard DL, Raichle ME, d-Avossa G (2012) [Dissociated mean and functional connectivity BOLD signals in visual cortex during eyes closed and fixation](#). J. Neurophysiol. In press. PMID 22875902
- Gates, K. M. [Identifying subgroups using fMRI connectivity maps](#). Annual Conference for the Society for Neuroscience, New Orleans, USA, October 13-18, 2012
- Molenaar, P. C. M. and Gates, K. M. A high precision method to estimate effective connectivity networks at the group and individual levels. World Congress for the International Organization of Psychophysiology, Pisa, Italy, September 13-17, 2012
- Alpay Özcan, [Complete Fourier Direct Magnetic Resonance Imaging \(CFD-MRI\) Equations for Diffusion MRI Signal](#), CDMRI’12, MICCAI 2012 Workshop on Computational Diffusion MRI, the 15th International Conference on Medical Image Computing and Computer Assisted Intervention, Nice, France, 1-5 October 2012.
- Alpay Özcan, Kenneth H. Wong, Linda Larson-Prior, Zang-Hee Cho, Seong K. Mun: [Background and Mathematical Analysis of Diffusion MRI Methods](#), International Journal of Imaging Systems and Technology, Feb. 2012, Vol. 22, pp. 44–52
- Alpay Özcan, James D. Quirk, Yong Wang, Qing Wang, Peng Sun, William M. Spees and Sheng--Kwei Song, [The Validation of Complete Fourier Direct MR Method for Diffusion MRI via Biological and Numerical Phantoms](#), pp.3756-3759, 33rd Annual International Conference of the IEEE EMBS, Boston, Massachusetts USA, August 30 - September 3, 2011
- Dr. Özcan has initiated the research topic in Frontiers in Physiology, Integrative Neuroscience: [New Models of Diffusion Weighted MRI Signal for Characterization of White Matter Integrity](#)
- Dr. Özcan was the invited speaker at McLean Hospital, Harvard Medical School, Belmont MA, Neuroscience Seminar Series in June 2012. He presented white matter integrity and its measurement with the Complete Fourier Direct MRI.
- Dr. Özcan was an invited speaker at Instituto San Lazaro de Neurociencias’ Inaugural Symposium, Circulo Medico Salta, Argentina, March 28-29, 2012. His presentation was on diffusion MR’s limitations in measuring the white matter integrity with specifics to neurological disorders.
- Dr. Özcan was an invited speaker at NRI-UPenn Joint Mini Symposium, Neuroscience Research Institute, Gacheon University Incheon, Korea on Sept 27-28, 2011 where he presented the new diffusion MRI model: Complete Fourier Direct MRI.
- Workshop: Study of Neuro-Stress with MRI Tractography and PET Imaging, Neuroscience Research Institute, Gacheon University Incheon, Korea, Feb 16-17, 2012

Conclusion

In anticipation of upcoming data from Gachon team, we have designed an appropriate PET imaging protocol that will allow us to differentiate regional metabolic activity between different sleep cycle periods. Clarification of timing methodology for double injection PET studies constitutes an important step towards accurate data acquisition, analysis and interpretation of results. As the time period between sleep cycles creates inter- and intra- subject variability, the variable decay amount of the contrast agent can potentially lead to inconclusive data acquisition. The establishment of the protocol will lead to more accurate and precise analysis and interpretation of future findings after the start of data collection awaiting IRB approval completion.

Pilot diffusion MRI data have been collected using a fixed human brain in order to apply the new and more accurate mathematical model, CFD-MRI, to MR acquisition for tractography. The analysis indicates the necessity of further investigations for better understanding and quantifying various artifacts in data collection. The information and deeper understanding of anatomy and white matter connectivity will lay the foundation of metabolic and dynamic functional changes within the brain. The microstructural form described by the diffusion MRI is necessary for a complete understanding of brain function. Therefore, the improvements towards a higher accuracy of diffusion MRI, rely on understanding and eliminating the artifacts, perturbation errors and their propagation in diffusion MR acquisition. CFD-MRI is tackling these important issues by going back to the origins of signal formation and addressing the fundamental modeling challenges.

Using the simultaneous fMRI-EEG techniques, brain regions of interest and their activity has been identified. The results of these studies clearly indicate changes in resting state brain network connectivity in the transition from alert wakefulness to sleep. An important change lay in the relationship between the default mode network and two networks involved in attending to and interacting with external stimuli. Further data collection will provide us with better description of the relationship between the default network and the peripheral networks that are activated during sleep cycles.

“So What” Section:

As the plenary speakers of the workshop have indicated, the outcomes of this Neuroperformance project, which is built on convergence of different disciplines, will have significant implications not only for warfighters but also the general population. Specifically our understanding of form via high resolution anatomical images and diffusion MRI tractography (with information on white matter integrity) using 7T MRI scanners and our understanding of function, including metabolic activity (via PET), BOLD activity (via fMRI) and electrical activity (via EEG), are essential to a neurobiologically informed approach to improvements in neuroperformance under conditions of restricted sleep and high stress. In addition to improving our understanding of the effects of stress and sleep loss on performance, and to providing a firmer understanding of the effects of pharmacological interventions under these conditions, these studies will provide novel data on the multifactorial impact of sleep loss, stress and cognitive load in the development of neuropsychiatric disorders commonly associated with abnormalities of sleep such as depression and anxiety.

References

1. A. Özcan, in *Engineering in Medicine and Biology Society (EMBC), 2010 Annual International Conference of the IEEE*. (2010), pp. 2710-2713.
2. A. Özcan, Comparison of the Complete Fourier Direct MRI with existing diffusion weighted MRI methods. *Biomedical Imaging: From Nano to Macro, 2011 IEEE International Symposium on*, 931 (March 30 2011-April 2 2011, 2011).
3. A. Özcan *et al.*, in *Engineering in Medicine and Biology Society, EMBC, 2011 Annual International Conference of the IEEE*. (2011), pp. 3756-3759.
4. A. Özcan, in *Workshop on Computational Diffusion MRI, MICCAI 2012 Medical Image Computing and Computer Assisted Intervention*. (Springer Verlag, Nice France, 2012).
5. A. Özcan, K. H. Wong, L. Larson-Prior, Z.-H. Cho, S. K. Mun, Background and mathematical analysis of diffusion MRI methods. *International Journal of Imaging Systems and Technology* **22**, 44 (2012).
6. S.-H. Oh *et al.*, Distortion correction in EPI at ultra-high-field MRI using PSF mapping with optimal combination of shift detection dimension. *Magnetic Resonance in Medicine* **68**, 1239 (2012).
7. L. J. Larson-Prior *et al.*, in *Progress in Brain Research*, E. J. W. V. Someren, Y. D. V. D. Werf, P. R. Roelfsema, H. D. Mansvelder, F. H. L. D. Silva, Eds. (Elsevier, 2011), vol. Volume 193, pp. 277-294.
8. M. E. Raichle *et al.*, A default mode of brain function. *Proceedings of the National Academy of Sciences* **98**, 676 (January 16, 2001, 2001).
9. J. R. Andrews-Hanna, J. S. Reidler, C. Huang, R. L. Buckner, Evidence for the Default Network's Role in Spontaneous Cognition. *Journal of Neurophysiology* **104**, 322 (July 1, 2010, 2010).
10. M. Corbetta, G. L. Shulman, Control of goal-directed and stimulus-driven attention in the brain. *Nat Rev Neurosci* **3**, 201 (03//print, 2002).
11. N. U. F. Dosenbach *et al.*, Distinct brain networks for adaptive and stable task control in humans. *Proceedings of the National Academy of Sciences* **104**, 11073 (June 26, 2007, 2007).
12. M. D. Fox *et al.*, The human brain is intrinsically organized into dynamic, anticorrelated functional networks. *Proceedings of the National Academy of Sciences of the United States of America* **102**, 9673 (July 5, 2005, 2005).
13. M. McAvoy *et al.*, Dissociated mean and functional connectivity BOLD signals in visual cortex during eyes closed and fixation. *Journal of Neurophysiology*, (August 8, 2012, 2012).

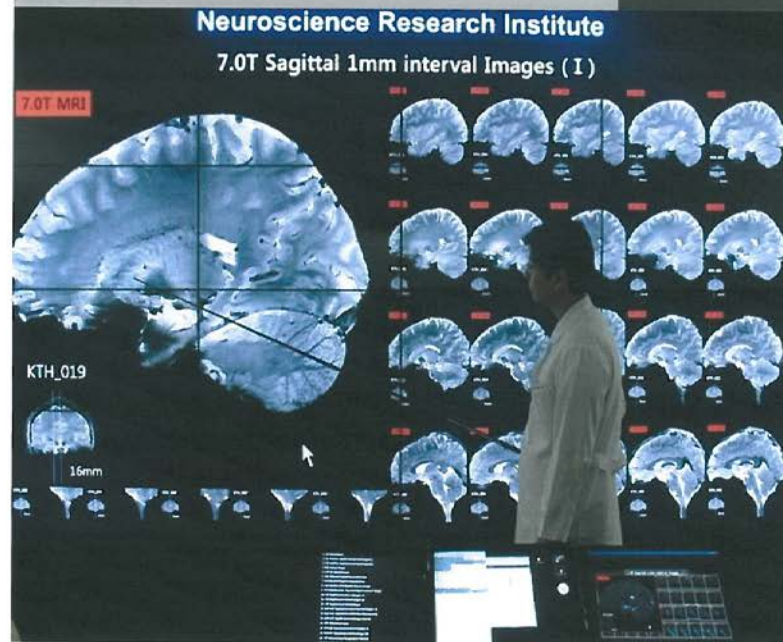


Neuroscience Research Institute
Gachon University of Medicine and Science, Incheon, Korea

International Workshop

Study of Neuro-Stress with MRI Tractography and PET Imaging

Symposium Chair : Zang-Hee Cho (NRI / Gachon Univ.)
 Co-Symposium Chair : Seong-Ki Mun (Washington Univ.)
 Local Program Chair : Young-Bo Kim (NRI / Gachon Univ.)



February 16th (Thur) - 17th (Fri), 2012

* Feb 16th (8:30AM ~ 06:00PM) / Feb 17th (8:30AM ~ 12:30AM)

Seminar room(5th Floor)

Neuroscience Research Institute, Incheon, KOREA

Neuroscience
Research
Institute

NRI

**International Workshop
Study of Neuro-Stress with
MRI Tractography and PET Imaging**

Neuroscience Research Institute, Gachon University
Inchon, Korea
Feb 16-17, 2012

Workshop Convener(s)

Zang-Hee Cho, Ph.D.,

University Professor & Director,

Neuroscience Research Institute, Gachon University of Medicine & Science, Korea

Seong Ki Mun, Ph.D.,

Director, Health Research Arlington Innovation Center, Virginia Tech, USA

Invited Speakers –

● **Zang-Hee Cho, Ph.D.,**

University Professor & Director, Neuroscience Research Institute,
Gachon University of Medicine & Science, Korea

“Advances in Neuro-imaging Instrumentation and Applications”

● **Col. Karl Friedl, Ph.D.,**

Director, U.S. Army Medical Research & Materiel Command’s (USAMRMC) Telemedicine &
Advanced Technology Research Center, (TATRC), USA

“Science and Assessment of Neuroperformance in Military Personnel”

● **Col. Christian Macedonia, M.D.,**

Program Manager, Defense Sciences Office, DARPA, USA

“Models of Multiple Stressors on the Brain of Warfighters”

● **Seog-Ju Kim, MD.,**

Seoul National University, Korea

“Neuroimaging studies on psychological trauma in Korea: application of 7.0 T MRI for trauma research ”

● **Hee-Sup Shin, MD, Ph.D.,**

Korea Institute of Science and Technology, Korea

“Selective Removal of Memory of Traumatic Incident in Mouse Model”

● **Linda Larson-Prior, Ph.D.,**

Electrical and Optical Imaging laboratory, Washington University, USA

“Introduction to Macro-Connectomics: Future Prospects”

● **Young-Don Son, Ph.D.,**

Neuroscience Research Institute, Korea

“Progress in Sleep Research”

● **Se-Hong Oh, Ph.D.,**


Dept. of Radiology, University of Pennsylvania, USA

“Methods for Diffusion Weighted Imaging at 7T MRI”

● **Alpay Özcan, D.Sc.,**

Health Research Arlington Innovation Center, Virginia Tech, USA

“Analysis of DW-MRI Signal for Fiber Measurements”

International Workshop (Study of Neuro-Stress with MRI Tractography and PET Imaging)			
Thursday Feb 16, 2012			
8:30AM	Welcoming Remarks • Zang-Hee Cho, Ph.D., Neuroscience Research Institute, Korea • Seong K. Mun, Ph.D., Arlington Innovation Center: Health Research, Virginia Tech, USA	3:00PM-3:30PM	Break
8:45AM - 9:15AM	Neurological and Mental Health in 2012 •LG. (ret). James Peake, MD Former Secretary of Department of Veterans' Affairs Former US Army Surgeon General (This presentation will be given via Conference Call Originating from Washington DC at 7:45 pm, Wednesday, Feb 15, 2012)	3:30PM	Analysis of DW-MRI Signal for Fiber Measurements • Alpay Özcan, D.Sc., Arlington Innovation Center: Health Research, Virginia Tech, USA
9:15AM - 10:00AM	Science and Assessment of Neuroperformance in the Military •COL. Karl Friedl, Ph.D. Director, Telemedicine & Advanced Technology Research Center US Army	4:15PM - 5:00PM	Progress in Sleep Research • Young-Don Son, Ph.D. Neuroscience Research Institute, Korea • Linda Larson-Prior, Ph.D. Washington University, St. Louis, USA
10:00AM - 10:15AM	Break	5:00PM – 5:45PM	Introduction to Macro-Connectomics: Future Prospects • Linda Larson-Prior, Ph.D. Electrical and Optical Imaging Laboratory Washington University, USA
10:15AM - 11:00AM	Advances in Neuro-imaging and Applications • Zang-Hee Cho, Ph.D., Neuroscience Research Institute, Korea	6:00PM	Banquet Dinner
11:30AM - 12:10PM	Methods for Diffusion Weighted Imaging at 7T MRI •Se-Hong Oh, Ph.D. Dept. of Radiology, University of Pennsylvania, USA	Friday, Feb 17, 2012	
12:10PM	Lunch Break	8:30AM	Summary Observation of the first day • Linda Larson-Prior, PhD • Alpay Özcan, D.Sc.,
1:30PM - 2:15PM	Selective Removal of Memory of Traumatic Incident in Mouse Model • Hee-Sup Shin, MD, Ph.D Korea Institute of Science and Technology, Korea	9:00AM	Models of Multiple Stressors on the Brain of Warfighters •COL. Christian Macedonia, M.D., Program Manager, Defense Sciences Office, DARPA, USA
2:15PM - 3:00PM	Neuroimaging studies on psychological trauma in Korea: application of 7.0 T MRI for trauma research Seog-Ju Kim, MD Seoul National University	9:30AM	Exploring the Ways Ahead, Research Strategy Facilitated Discussion • Seong K. Mun, Ph.D. •COL. Karl Friedl, PhD
		12:30PM	Closing Remarks & Adjournment • Zang-Hee Cho, Ph.D. and Seong K. Mun, Ph.D.

Appendix 2
Complete Fourier Direct Magnetic Resonance Imaging (CFD–MRI) Equations for Diffusion
MRI Signal

Complete Fourier Direct Magnetic Resonance Imaging (CFD–MRI) Equations for Diffusion MRI Signal

Alpay Özcan

Health Research, Arlington Innovation Center,
Virginia Polytechnic Institute and State University, 900 N. Glebe Road, Arlington
VA, 22203, USA.,
alpay@vt.edu
<http://www.aic.ncr.vt.edu>

Abstract. By carefully re-examining the first principles of diffusion weighted magnetic resonance imaging (DW–MRI) signal formation and deriving the mathematical model from scratch, the foundation for an accurate and unifying Fourier based theory is constructed. The derivations are specifically obtained for DW–MRI signal by including imaging gradients and without taking the magnitude of the signal using particle methods instead of the conventional partial differential equations approach. The signal is shown to be the Fourier transform of the joint distribution of number of the magnetic moments (at a given location at the initial time) and their displacement integrals which augments the k -space by three more dimensions. The joint distribution function is recovered by applying the Fourier transform to the complete high-dimensional data set. A physically meaningful real valued distribution function is obtained after phase corrections are applied for the re-establishment of Hermitian symmetry in the signal. Consequently, the method is fully unconstrained and directly presents the distribution of displacement integrals without any assumptions such as symmetry or Markovian property. The joint distribution function is visualized with isosurfaces overlaid on the distribution map of the number of magnetic moments with low mobility. The presentation provides a highly detailed level of microstructural information. The results are demonstrated on the experimental data obtained from an ex-vivo baboon brain.

Keywords: magnetic resonance imaging, diffusion weighted imaging, Fourier transform

1 Introduction

Diffusion weighted (DW) MRI's ability to estimate molecular displacements provides information about the microstructure within which the motion takes place. The technique has successfully been used in a variety of clinical and research

areas such as cancer diagnosis [1], white matter integrity assessment [2], in monitoring of neurological diseases such as multiple sclerosis [3] and disorders [4] as well as neonatal development [5].

However, the existence of several methods for modeling the DW–MRI signal is proof that the field has not yet reached a satisfactory consensus. A thorough mathematical analysis and a description of the subject and the background of existing methods is presented in [6]. Herein, to provide a unified approach, the MRI signal in the presence of diffusion sensitizing gradients is derived by carefully re-examining the first principles of DW–MRI signal formation and deriving the mathematical model from scratch using particle methods in the spirit of the work of McCall et al. [7] rather than starting from the conventional partial differential equations (PDE) of Stejskal and Tanner [8]. The outcome is the Complete Fourier Direct (CFD) MRI method [9] that establishes a high dimensional Fourier relationship between the signal and the joint distribution of position and displacement integrals of the particles.

2 Signal Formation

The derivation of the CFD–MR signal model is accomplished by simply expressing the magnetization of each magnetic moment. For this purpose, the effect of spin–spin relaxation can be neglected. The evolution of the transverse magnetization of the i^{th} magnetic moment is described in a standard manner by a rotating magnetization vector:

$$m_i(t) = \exp(-j\gamma\Omega_i) m_i(t_0). \quad (1)$$

Here, γ is the gyromagnetic ratio, the transverse magnetization vector, m_i , is written in complex number form with $m_i(t_0)$ denoting the initial magnetization tipped to the transverse plane,

$$\Omega_i = \int_{t_0}^t G(x_i, \tau) \cdot x_i(\tau) d\tau \quad (2)$$

describes the phase as a function of the magnetic field gradients $G(x, t) \in \mathbb{R}^3$, and the position of the magnetic moment is $x_i \in \mathbb{R}^3$.

The signal originates from all of the magnetic moments

$$M(t) = \sum_i m_i(t) = \sum_i \exp(-j\gamma\Omega_i) m_i(t_0). \quad (3)$$

In order to precisely obtain the CFD–MR signal, the time evolution of the phase, Ω_i , in Eq. 2 must be explicitly written on the right hand side of Eq. 3 by expressing x_i . The time dependent position of each magnetic moment is given as:

$$x_i(t) = x_i(t_0) + w_i(t) \quad (4)$$

where $w_i(t) \in \mathbb{R}^3$ represents the displacement of the magnetic moment from its initial position with $w_i(t_0) = 0$. The function $w_i(t)$ could express any kind of displacement such as Brownian motion, molecular movement in biological tissue with different medium and obstacles, coherent motion or any combination thereof. The function does not have to be differentiable but it must be continuous to make physical sense since a magnetic moment cannot disappear at a given point and reappear at another. No other requirements and/or assumptions about motion properties in the time domain, deterministic and/or stochastic, such as being Markovian, is required in the derivations of the CFD model. Based on

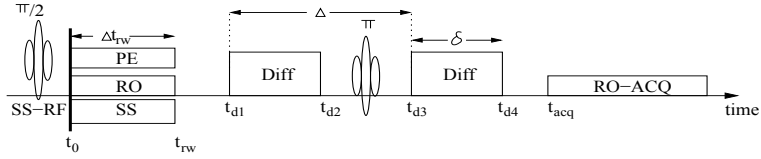


Fig. 1. The pulsed–gradient spin–echo (PGSE) pulse sequence and the definition of the variables used in the calculations. RO is for read out, PE for phase encode, SS for is the slice select gradient, Diff marks the motion sensitizing pulses and ACQ stands for digital acquisition period. In practice, the MR pulse sequences implement the rewind (rw) gradients such that the amplifiers are turned on and off at the same times. The magnetic field gradient pulses during the radio frequency (RF) pulses are not shown because their effect is overwhelmed by the RF pulse (see also the text).

this model, the phase of the i^{th} magnetic moment during the digital acquisition period of the pulsed–gradient spin–echo (PGSE) sequence of Fig. 1 (for $l_{\text{mr}} = 2$ dimensional imaging slice) is obtained after tedious but routine derivations as follows. In the beginning of each acquisition, a $\pi/2$ radio frequency (RF) pulse tips the longitudinal magnetization to the transversal plane. The initial time, t_0 , is chosen accordingly to be the end time of the RF pulse when the magnetization is fully tipped to the transversal plane. Using the definitions of the variables in Fig. 1, the evolution of the phase is described as:

1) First, imaging gradients for read out rewinding, $G_{\text{ro}} \in \mathbb{R}^3$, phase encoding, $G_{\text{pe}} \in \mathbb{R}^3$ and slice select $G_{\text{ss}} \in \mathbb{R}^3$ on the time interval $[t_0, t_{\text{rw}}]$ are turned on. After these gradients are applied the phase and the magnetization become

$$\begin{aligned}
 \Omega_{\text{rw}} &= \int_{t_0}^{t_{\text{rw}}} (G_{\text{ro}}(\tau) + G_{\text{pe}}(\tau) + G_{\text{ss}}(\tau)) \cdot x_i(\tau, t_0) d\tau \\
 &= (G_{\text{ro}} + G_{\text{pe}} + G_{\text{ss}}) \cdot \left(\Delta t_{\text{rw}} x_i(t_0) + \int_{t_0}^{t_{\text{rw}}} w_i(\tau) d\tau \right) \\
 &= \Delta t_{\text{rw}} (G_{\text{ro}} + G_{\text{pe}} + G_{\text{ss}}) \cdot x_i(t_0)
 \end{aligned}$$

$$+(G_{\text{ro}} + G_{\text{pe}} + G_{\text{ss}}) \cdot \int_{t_0}^{t_{\text{rw}}} w_i(\tau) d\tau. \quad (5)$$

Note that the calculations are carried out assuming ideal gradient amplifiers resulting in rectangular shaped gradient pulses in the formulation. Routine derivations for trapezoidal shapes are omitted for clarity.

2) The π RF pulse between the diffusion gradient pulses, $G_{\text{D}} \in \mathbb{R}^3$, and the accompanying slice select gradient provide theoretical sign reversal of the phase. The slice select gradient during this period does not encode magnetic moment motion into the signal (thus it is not shown in Fig. 1). This is a direct consequence of the RF pulse imposes a strong magnetic field that changes all of the entries of the main magnetic field B_0 . In comparison, the slice select gradient's modification of the third component of the B_0 vector is negligible. Therefore the strong (RF) magnetic field rotates the magnetization vector m_i of each magnetic moment without being affected by diffusion.

Since $x_i(t_{dk}) = x_i(t_0) + w_i(t_{dk})$, $k = 1, \dots, 4$; at $t = t_{d4}$

$$\begin{aligned} \Omega_{\text{D}} &= \int_{t_{d3}}^{t_{d4}} G_{\text{D}} \cdot x_i(\tau, t_0) d\tau - \int_{t_{d1}}^{t_{d2}} G_{\text{D}} \cdot x_i(\tau, t_0) d\tau \quad (6) \\ &= G_{\text{D}} \cdot \left((t_{d4} - t_{d3}) x_i(t_0) + \int_{t_{d3}}^{t_{d4}} w_i(\tau) d\tau \right) \\ &\quad - G_{\text{D}} \cdot \left((t_{d2} - t_{d1}) x_i(t_0) + \int_{t_{d1}}^{t_{d2}} w_i(\tau) d\tau \right) \\ &= G_{\text{D}} \cdot \left(\int_{t_{d3}}^{t_{d4}} w_i(\tau) d\tau - \int_{t_{d1}}^{t_{d2}} w_i(\tau) d\tau \right) \\ &\quad + ((t_{d4} - t_{d3}) - (t_{d2} - t_{d1})) G_{\text{D}} \cdot x_i(t_0). \quad (7) \end{aligned}$$

The sign change on Ω_{rw} is the effect of the π pulse, which is incorporated in the expression for Ω_{D} . If the diffusion gradient times are equal, i.e., $t_{d4} - t_{d3} = t_{d2} - t_{d1} = \delta$, then the last term in Eq. 7 is equal to zero, erasing the influence of initial position from motion encoding part of the signal. As a result, the formulation with displacement integrals, $\int w_i(\tau) d\tau$, is a more meaningful choice than the center of mass (COM) of random walk, $\int x(\tau) d\tau$, introduced in [10].

3) The last part of the sequence is where the data are collected:

$$\Omega_{\text{ro}}(t) = \int_{t_{\text{acq}}}^t G_{\text{ro}} \cdot (x_i(t_0) + w_i(\tau)) d\tau = (t - t_{\text{acq}}) G_{\text{ro}} \cdot x_i(t_0) + \int_{t_{\text{acq}}}^t G_{\text{ro}} \cdot w_i(\tau) d\tau, \quad (8)$$

$$\Omega_i(t, G_{\text{pe}}, G_{\text{ss}}, G_{\text{D}}) =$$

$$(t - t_{\text{acq}} - \Delta t_{\text{rw}}) G_{\text{ro}} \cdot x_i(t_0) - \Delta t_{\text{rw}} G_{\text{pe}} \cdot x_i(t_0) - \Delta t_{\text{rw}} G_{\text{ss}} \cdot x_i(t_0) + G_{\text{D}} \cdot W^{\text{d}} + G_{\text{ro}} \cdot W_i^{\text{acq}}(t) - (G_{\text{ro}} + G_{\text{pe}} + G_{\text{ss}}) \cdot W_i^{\text{rw}} \quad (9)$$

Equation 9 incorporates three integrals of the displacement $w_i(t) : (W_i^{\text{d}}, W_i^{\text{acq}}, W_i^{\text{rw}})$ corresponding to the displacement integrals for diffusion (d), analog to digital conversion acquisition (acq) and initial rewind (rw) gradient time periods respectively

$$W_i^{\text{d}} = \int_{t_{\text{d3}}}^{t_{\text{d4}}} w_i(\tau) d\tau - \int_{t_{\text{d1}}}^{t_{\text{d2}}} w_i(\tau) d\tau, \quad W_i^{\text{acq}}(t) = \int_{t_{\text{acq}}}^t w_i(\tau) d\tau, \quad W_i^{\text{rw}} = \int_{t_0}^{t_{\text{rw}}} w_i(\tau) d\tau. \quad (10)$$

Moreover, in Eq. 9, the first two terms that multiply the initial position $x_i(t_0)$ are the foundation of MR imaging and can be written in the k -space formalism as

$$k_{\text{mr}}(t, G_{\text{pe}}) = (t - t_{\text{acq}} - \Delta t_{\text{rw}}) G_{\text{ro}} - \Delta t_{\text{rw}} G_{\text{pe}} \quad (11)$$

where G_{ro} and Δt_{rw} are fixed, and t and G_{pe} define the sampling points in k -space. Also, the term $\varphi_{\text{slice}} = -\Delta t_{\text{rw}} G_{\text{ss}} \cdot x_i(t_0)$ is constant for all i because the slice select axis component of $x_i(t_0)$ is the slice position.

Without loss of generality, the coordinate frame used for the equations is the imaging coordinate frame defined by the read-out, phase encode and slice select gradients, $G_{\text{ro}} = [g_{\text{ro1}}, 0, 0]$, $G_{\text{pe}} = [0, g_{\text{pe2}}, 0]$, $G_{\text{ss}} = [0, 0, g_{\text{ss3}}]$. Using this notation, Eq. 11 implies that $t = k_{\text{mr1}}/g_{\text{ro1}} + t_{\text{acq}} + \Delta t_{\text{rw}}$ and $g_{\text{pe2}} = -k_{\text{mr2}}/\Delta t_{\text{rw}}$ where k_{mr} has its components equal to

$$[k_{\text{mr1}}, k_{\text{mr2}}, k_{\text{mr3}}] = [(t - t_{\text{acq}} - \Delta t_{\text{rw}}) g_{\text{ro1}}, -\Delta t_{\text{rw}} g_{\text{pe2}}, 0].$$

With this, $W_i^{\text{acq}}(t)$ becomes a function of k_{mr1} and it is denoted by $W_i^{\text{acq}}(k_{\text{mr1}})$. The coefficients of W^{rw} in Eq. 9 are written as a vector:

$$k_{\text{rw}} = [-g_{\text{ro1}}, k_{\text{mr2}}/\Delta t_{\text{rw}}, -g_{\text{ss3}}], \quad (12)$$

which is an *affine* function of k_{mr} .

By defining $k_{\text{D}} = G_{\text{D}}$, Eq. 9 is rewritten concisely:

$$\Omega_i = k_{\text{mr}} \cdot x_i(t_0) + k_{\text{D}} \cdot W_i^{\text{d}} + k_{\text{rw}} \cdot W_i^{\text{rw}} + W_{i,1}^{\text{acq}}(k_{\text{mr1}}) g_{\text{ro1}} + \varphi_{\text{slice}}, \quad (13)$$

reflecting the partition of the effect of initial position and displacement integrals on the phase of each magnetic moment. Since φ_{slice} is constant for all i , it is taken out of Eq. 13 with the appropriate rotation of the magnetization coordinate frame on a slice by slice basis.

In Eq. 13, the pairs $(k_{\text{mr}}, x_i(t_0))$, $(k_{\text{D}}, W_i^{\text{d}})$ and $(k_{\text{rw}}, W_i^{\text{rw}})$ are clearly Fourier dual variables while W_i^{acq} introduces dependence on magnetic moment motions. The derivations of the total signal expression in the next section clarifies this Fourier relationship.

3 Complete Fourier Direct MRI

The total CFD–MRI signal comes from all of the magnetic moments and it is the sum of individual magnetizations with the real valued initial magnetization $m_i(t_0) = m_0$. Equation 3 can be re–written using the relationship in Eq. 13 using the Fourier variables of Section 2:

$$S_{\text{cfd}}(k_{\text{mr}}, k_{\text{D}}, k_{\text{rw}}) = m_0 \sum_i \exp(-j\gamma \Omega_i(k_{\text{mr}}, k_{\text{D}}, k_{\text{rw}})). \quad (14)$$

The dimension of the signal domain is $(l_{\text{mr}} + 3 + 3)$ but, whereas $(k_{\text{mr}}, k_{\text{D}}) \in \mathbb{R}^{l_{\text{mr}}+3}$ are independent variables, $k_{\text{rw}} \in \mathbb{R}^3$ is affinely dependent on k_{mr} by Eq. 12. Accordingly, the CFD k –space variable is defined by joining the independent variables: $k_{\text{cfd}} = (k_{\text{mr}}, k_{\text{D}}) \in \mathbb{R}^{l_{\text{mr}}+3}$.

Since the properties of interest, e.g., tissue structure, are location dependent, instead of adding up the magnetization magnetic moment by magnetic moment, the sum in Eq. 14 can be carried out in *the joint position–displacement integral space*. For this purpose, the total CFD distribution function, $P_{\text{cfd}}^{\text{total}}(x, W)$, is defined here as the number of magnetic moments with the initial position $x \in \mathbb{R}^3$ at time t_0 , possessing the displacement integral values of $W = (W^{\text{d}}, W^{\text{rw}}, W_1^{\text{acq}}) \in \mathbb{R}^7$. By definition, $P_{\text{cfd}}^{\text{total}}$ is real valued and positive semi–definite.

All of the individual magnetic moment signals coming from the infinitesimal volume element $dx dW$ around the (position, displacement integral) point (x, W) must be integrated to form the DW–MRI signal. The sum in Eq. 14 becomes (absorbing m_0 into $P_{\text{cfd}}^{\text{total}}$ for ease of notation):

$$S_{\text{cfd}}(k_{\text{mr}}, k_{\text{D}}, k_{\text{rw}}) = \int P_{\text{cfd}}^{\text{total}}(x, W) \times \exp(-j\gamma(k_{\text{mr}} \cdot x + k_{\text{D}} \cdot W^{\text{d}} + k_{\text{rw}} \cdot W^{\text{rw}} + W_1^{\text{acq}}(k_{\text{mr}1})g_{\text{ro}1})) dx dW \quad (15)$$

defining the Fourier transform of the total CFD distribution function $P_{\text{cfd}}^{\text{total}}$ evaluated at the frequencies specified by $(k_{\text{mr}}, k_{\text{D}}, k_{\text{rw}})$:

$$S_{\text{cfd}}(k_{\text{mr}}, k_{\text{D}}, k_{\text{rw}}) = \mathcal{F}\{P_{\text{cfd}}^{\text{total}}\}(k_{\text{mr}}, k_{\text{D}}, k_{\text{rw}}) \quad (16)$$

with nonlinearities added by W_1^{acq} . Accordingly, the only physical constraint that guides the signal reconstruction is the following.

Since $P_{\text{cfd}}^{\text{total}}$ is real valued, S_{cfd} is Hermitian symmetric.

Experimentally, $P_{\text{cfd}}^{\text{total}}$ cannot be obtained by the inversion of Eq. 16 *via* discrete Fourier transform (DFT) because k_{rw} cannot be independently sampled at necessary points (e.g., on a Cartesian grid) due to the affine dependence of k_{rw} on k_{mr} in Eq. 12. However, $P_{\text{cfd}}^{\text{total}}$ is not the main point of interest for discovering the microstructural properties of the environment. Among the elements of W , the focus is on the most descriptive MRI observable, W^{d} . The objective is to marginalize W^{rw} from Eq. 15 to obtain the distribution

$$P_{\text{cfd}}(x, W^{\text{d}}) = \int P_{\text{cfd}}^{\text{total}}(x, W^{\text{d}}, W^{\text{rw}}) dW^{\text{rw}} = \mathcal{F}_{(k_{\text{mr}}, k_{\text{D}})}^{-1}\{S_{\text{cfd}}(k_{\text{mr}}, k_{\text{D}}, 0)\}. \quad (17)$$

without being able to sample at $k_{\text{rw}} = 0$.

With this issue at hand and the disruption of the Hermitian property of $S_{\text{cfd}}(k_{\text{mr}}, k_{\text{D}}, k_{\text{rw}})$ (and therefore $S_{\text{cfd}}(k_{\text{mr}}, k_{\text{D}}, 0)$) under experimental conditions, the estimation of P_{cfd} is achieved by applying systematic phase corrections during the computation of the transform in Eq. 17. By refraining from using the signal’s magnitude both the energy and information content are simultaneously preserved also permitting asymmetry in P_{cfd} . The starting point the regular spin-echo image: $I_{k_{\text{mr}}}^{\text{complex}}((x_{\text{ro}}, x_{\text{pe}}), 0, k_{\text{rw}}) = \mathcal{F}_{k_{\text{mr}}}^{-1}\{S_{\text{cfd}}(k_{\text{mr}}, 0, k_{\text{rw}})\}$. The theoretically real valued image $I_{k_{\text{mr}}}$ becomes complex valued, $I_{k_{\text{mr}}}^{\text{complex}} = I_{k_{\text{mr}}} \exp(j \angle I_{k_{\text{mr}}}^{\text{complex}})$ due to the systematic echo time shifting from the middle of the read-out period that creates a linear phase shift in the physical read-out axis and other effects, such as motion, along the phase-encode axis. The phase shifts are approximated by polynomials in each imaging axis

$$r_{\text{ro}}(x_{\text{ro}}) \approx \angle I_{k_{\text{mr}}}^{\text{complex}}((x_{\text{ro}}, 0), 0), \quad r_{\text{pe}}(x_{\text{pe}}) \approx \angle I_{k_{\text{mr}}}^{\text{complex}}((0, x_{\text{pe}}), 0). \quad (18)$$

The corrections are then applied systematically at each value of k_{D} according to:

$$I_{k_{\text{mr}}}(x, k_{\text{D}}) = I_{k_{\text{mr}}}^{\text{complex}}(x, k_{\text{D}}) \exp(-j(r_{\text{ro}}(x_{\text{ro}}) + r_{\text{pe}}(x_{\text{pe}}))). \quad (19)$$

Afterwards, the Fourier transform in k_{D} -space,

$$P_{\text{cfd}}(x, W^{\text{d}}) = \mathcal{F}_{k_{\text{D}}}^{-1}\{I_{k_{\text{mr}}}(x, k_{\text{D}})\}, \quad (20)$$

is evaluated sequentially in each k_{D} -dimension. At each step before executing the transform, the Hermitian property in k_{D} -space is re-established, $I_{k_{\text{mr}}}(x, -k_{\text{D}}) = I_{k_{\text{mr}}}^*(x, k_{\text{D}})$ as demonstrated in Fig 2.

4 Experimental Setup and Analysis Methods

A fixed baboon brain immersed in 4% paraformaldehyde was used for the experiments. The primate was prematurely delivered on the 125th day and sacrificed on the 59th day after delivery. All animal husbandry, handling, and procedures were performed at the Southwest Foundation for Biomedical Research, San Antonio, Texas. Animal handling and ethics were approved to conform to American Association for Accreditation of Laboratory Animal Care (AAALAC) guidelines. Further details of the preparation are explained in [11].

The experiments were carried out on a 4.7 Tesla MR scanner (Varian NMR Systems, Palo Alto, CA, USA) with a 15 cm inner diameter gradient system, 45 Gauss/cm maximum gradient strength and 0.2 ms rise time using a cylindrical quadrature birdcage coil (Varian NMR Systems, Palo Alto, CA, USA) with 63 mm inner diameter.

CFD-MRI data were obtained using the standard pulsed-gradient spin-echo multi-slice sequence. The k_{mr} -space was sampled to result in images of 128×128 pixels with a field of view $64 \times 64 \text{ mm}^2$ and 0.5 mm slice thickness. The k_{D} -space was sampled in a uniformly spaced Cartesian grid in a cube

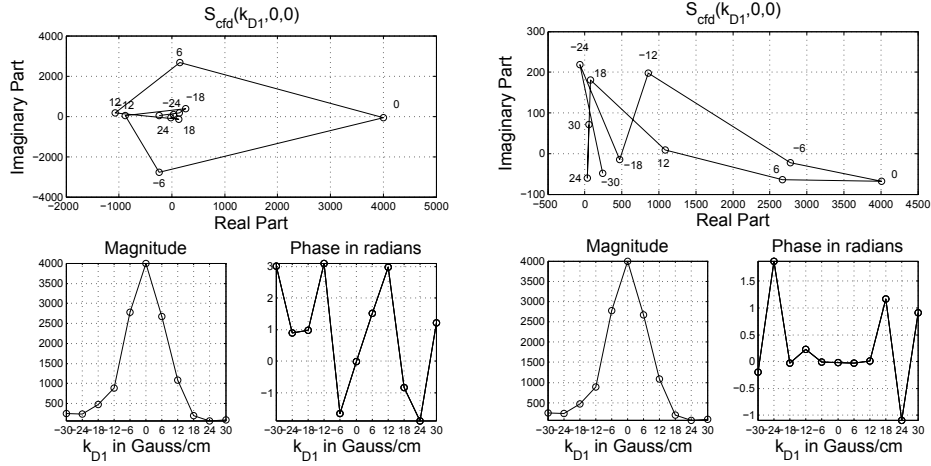


Fig. 2. On the top row the Nyquist plots of uncorrected (left) and corrected (right) S_{cfd} obtained from the experimental data described in Section 4. The plots show data acquired at each diffusion gradient value k_{D1} on the complex plane. On the bottom row are the magnitude and phase plots of the data. Uncorrected data (bottom row left, second column) exhibit a linear phase shift around 0 frequency, indicative of coherent motion. After the phase corrections obtained using the polynomial $0.266 k_{D1}$ estimated from the points $k_{D1} = -6, 0, 6, 12$ Gauss/cm, the magnitude is unchanged but signal's imaginary part is smaller for the corrected values visible in the vertical axis spans of Nyquist plots and the phase plots.

$[-30 \text{ Gauss/cm}, 30 \text{ Gauss/cm}]^3$ with $11 \times 11 \times 11$ voxels, i.e., 6 Gauss/cm sampling intervals at each dimension. In regular MRI terms, 1331 images per slice were obtained. The repetition time $T_R = 1$ s, echo time $T_E = 56.5$ ms, diffusion pulse time offset $\Delta = 30$ ms and diffusion pulse duration $\delta = 15$ ms were used.

After the acquisition, the data were transferred to a two quad core 2.3GHz Intel Xeon® cpu and 8GB memory Dell Precision Workstation 490 running Windows XP® 64-bit operating system. The DWI data were placed in a 5-dimensional array in the computer memory and the discrete Fourier transform was computed along with the phase corrections as recounted in Section 3. Afterwards, isosurfaces were computed as explained in Section 5. In-house Matlab® (Mathworks, Natick, MA USA) programs were used for all of the computations and to display the graphics and maps.

5 Visualization of the CFD Distribution

In the case of a two dimensional MR slice ($l_{\text{mr}} = 2$), the domain of P_{cfd} is the five dimensional real space $P_{\text{cfd}} : \mathbb{R}^{l_{\text{mr}}} \times \mathbb{R}^3 \rightarrow \mathbb{R}$, which makes the visualization challenging. The task is realized by using two components: the presentation of the number of magnetic moments at the initial position and the three

dimensional distribution of the displacement integral values. The former is accomplished by using $P_{\text{cfd}}(x, 0)$ as the background image, e.g., in Fig. 3, because in a restricted environment without coherent motion, the function $P_{\text{cfd}}(x, W^{\text{d}})$ assumes its maximum at $W^{\text{d}} = 0$ since the majority of the magnetic moments do not travel too far from their initial position. If there is coherent motion, linear portion of phase corrections rectify it anyway.

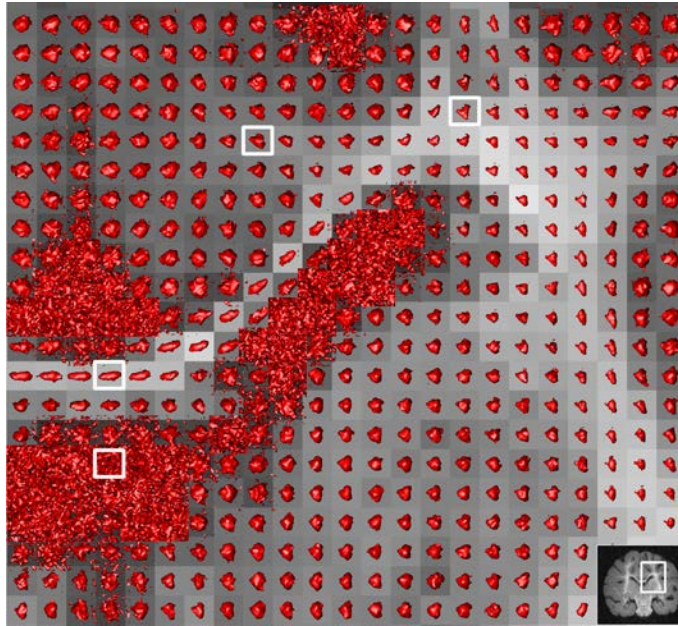


Fig. 3. The isosurfaces ($\bar{P}_{\text{cfd}} = 0.17$) picked from the area around the corpus colosum (CC) and external capsule (EC) junction. The area of interest is indicated on the right bottom corner. Starting from left bottom going clockwise, the sample pixels of Fig. 4 are from cerebrospinal fluid (CSF), CC, White Matter (WM) and CC and EC junction respectively. The isosurfaces for different c -values are shown in Fig. 4.

In order to present the displacement integral component with the sole purpose of obtaining a single scale across the image, P_{cfd} is normalized at each location x : $\bar{P}_{\text{cfd}}(x, W^{\text{d}}) = P_{\text{cfd}}(x, W^{\text{d}})/P_{\text{cfd}}(x, 0)$. The second part of visualization is achieved by overlaying on $P_{\text{cfd}}(x, 0)$ the isosurfaces of \bar{P}_{cfd} with a level value c ($0 < c \leq 1$), i.e. $\{W^{\text{d}} \in \mathbb{R}^3 : \bar{P}_{\text{cfd}}(x, W^{\text{d}}) = c\}$. For the sake of an objective assessment, a common c -value is adopted throughout the image after the normalization creating a different isosurface at each location. For biological tissue, relevant information is provided by the values of P_{cfd} away from $c = 0$, i.e., the outskirts of P_{cfd} corresponding to the small number of magnetic moments that travel further away, portraying the microstructure. The effect of level value choice is summarized in Fig. 4 displaying isosurfaces from four different pixels within the baboon brain marked in Fig. 3:

- 1) Too high values do not provide enough structural information (see the first rows in Fig. 4).
- 2) The appropriately informative value depends on the properties of the motion (thus of the microstructure) at a given location (compare the columns of Fig. 4).
- 3) Too low values force the isosurfaces to become extremely noisy (see last rows of Fig. 4).

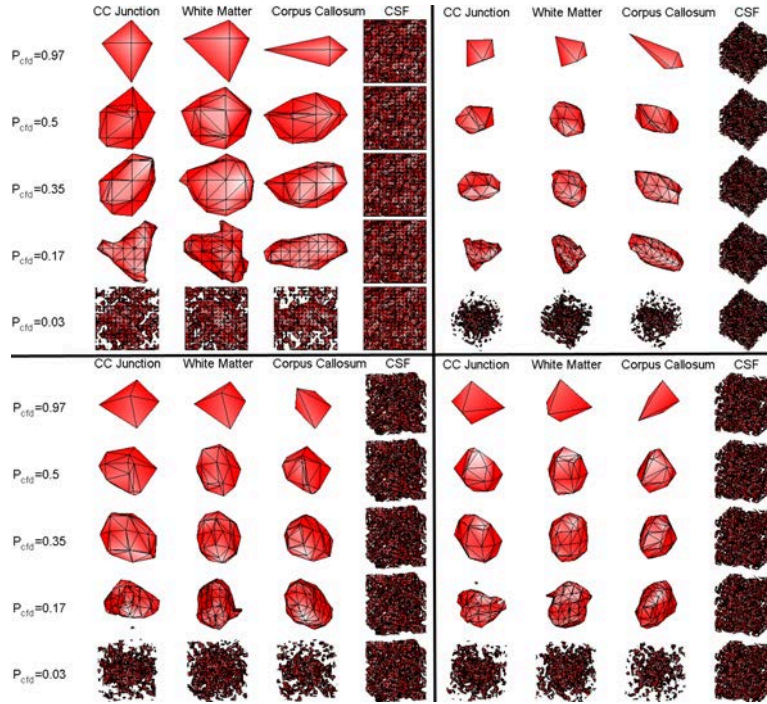


Fig. 4. Using multiple c -values, the isosurfaces from the area around the CC and EC junction marked in Fig. 3 are shown with different view angles in \mathbf{R}^3 at each subfigure in the quadrants. Less and less information is available with an increasing c -value. In contrast, if the value is chosen to be too low, all of the isosurfaces are immersed in noise. Regardless of the c -value, the CSF isosurface is noisy because the diffusion pulse times, which are appropriate for diffusion in tissue, are too long for the displacement in the fluid.

In Figs. 3 and 4, highly structured areas, e.g., the corpus callosum (CC), demonstrate ellipsoidal shapes. In contrast, at the junctions, the isosurfaces indicate crossing fibers (see the ‘T’ shaped isosurface in Fig. 4) at the CC–external capsule (EC) junction. The organization in white matter presents shapes in between. These properties are highly informative for tractographic studies.

Overall, the isosurfaces are not constrained to given forms like Gaussians, spherical harmonics or to any expansions. In fact, they are typically not even symmetric. They are general and direct.

6 Conclusion and Future Studies

CFD–MRI brings clarifications to the nature of the DW–MR signal as well as conceptual simplifications over existing methods [12]. The narrow pulse approximation (negligible duration of diffusion sensitizing magnetic field gradient pulse) is not necessary because CFD–MRI uses the displacement integrals, which incorporate directly pulse durations, rather than the displacements themselves. In other words, P_{cfd} does not involve the propagator which is the basis of spectral methods [13]. Furthermore, this also removes the necessity to model the motion as a stochastic process relieving in conjunction the constraints and derivations, such as being Markovian, in the existing methods.

The high dimensional Fourier relationship with the support of Hermitian property preservation (to avoid the usage of signal magnitude) results in completely free distribution functions that display asymmetry as demonstrated in Figs. 3 and 4 in an evidence based manner. Accordingly, re-establishment of Hermitian symmetry requires future development of more sophisticated systematic phase corrections starting from the ones introduced herein. From a practical point of view, this mathematically challenging task also requires a deeper investigation and better understanding of the origin of DW–MRI artifacts, specifically the ones that disturb the Hermitian property.

The clinical aim of future studies is the establishment of connections between biological properties and the CFD distribution function, P_{cfd} . The challenge is, therefore, the classification of different microstructures, healthy and pathological, despite lack of analytical descriptions of P_{cfd} for even simple geometries. A biological phantom, with known geometry, constructed with two nerve fiber bundles and agar gel has been recently investigated as an initial step towards that goal [14].

The analysis and visualization of P_{cfd} need to be designed to define and enhance CFD–MRI surrogate markers for diagnosis and prognosis of disease, in the mentality of the accomplishments with DTI markers in [3]. Naturally, these markers will provide much deeper information than the existing DW–MRI methods. However, the effect of integration on the displacement has to be carefully studied, for example, in order to make axon caliber assessments for white matter integrity estimation. Likewise, the observation that in DW–MRI the displacement is from the initial magnetic moment position indicates that fiber tractography methods cannot exactly determine the location of tracts within a pixel. It will be necessary to introduce new tools, e.g., from differential geometry, for better characterization, categorization and visualization of three dimensional motion portion of P_{cfd} .

Acknowledgement

This study was supported, in part, by the Washington University Small Animal Imaging Resource (U24-CA83060), the NIH/NINDS grant Biomarkers and Pathogenesis of MS (P01-NS059560), and the US Army grant, NeuroPerformance Imaging (W23RYX1089N603). Special thanks to J. Quirk, T. Conturo,

S-K. Song, K. Uğurbil, G. Sapiro, K. Wong, S. K. Mun and Z-H. Cho for valuable discussions.

References

1. Song, S.K., Qu, Z., Garabedian, E.M., Gordon, J.I., Milbrandt, J., Ackerman, J.J.H.: Improved magnetic resonance imaging detection of prostate cancer in a transgenic mouse model. *Cancer Research* **62**(5) (March 2002) 1555–1558
2. Budde, M.D., Kim, J.H., Liang, H.F., Schmidt, R.E., Russell, J.H., Cross, A.H., Song, S.K.: Toward accurate diagnosis of white matter pathology using diffusion tensor imaging. *Magnetic Resonance in Medicine* **57**(4) (April 2007) 688–695
3. Song, S.K., Sun, S.W., Ramsbottom, M.J., Chang, C., Russell, J., Cross, A.H.: Demyelination revealed through MRI as increased radial (but unchanged axial) diffusion of water. *NeuroImage* **17**(3) (November 2002) 1429–1436
4. Ciccarelli, O., Catani, M., Johansen-Berg, H., Clark, C., Thompson, A.: Diffusion-based tractography in neurological disorders: concepts, applications, and future developments. *The Lancet Neurology* **7**(8) (2008) 715–727
5. McKinstry, R.C., Mathur, A., Miller, J.H., Özcan, A., Snyder, A.Z., Schefft, G.L., Almlı, C.R., Shiran, S.I., Conturo, T.E., Neil, J.J.: Radial organization of developing preterm human cerebral cortex revealed by non-invasive water diffusion anisotropy MRI. *Cerebral Cortex* **12** (December 2002) 1237–1243
6. Özcan, A., Wong, K.H., Larson-Prior, L., Cho, Z.H., Mun, S.K.: Background and mathematical analysis of diffusion mri methods. *International Journal of Imaging Systems and Technology* **22**(1) (2012) 44–52
7. McCall, D.W., Douglass, D.C., Anderson, E.W.: Self-diffusion studies by means of nuclear magnetic resonance spin-echo techniques. *Berichte der Bunsengesellschaft für Physikalische Chemie* **67**(3) (1963) 336–340
8. Stejskal, E.O., Tanner, J.: Spin diffusion measurements: Spin echoes in the presence of a time-dependent field. *The Journal of Chemical Physics* **42**(1) (January 1965) 288–292
9. Özcan, A.: A new model for diffusion weighted MRI: Complete fourier direct MRI. In: *Proceedings of the 32st Annual International Conference of the IEEE EMB Society, Buenos Aires, Argentina (September 2010)* 2710–2713 PAP - EMBC10.1722.
10. Mitra, P.P., Halperin, B.I.: Effects of finite gradient-pulse widths in pulsed-field-gradient diffusion measurements. *Journal of Magnetic Resonance. Series A* **113**(1) (March 1995) 94–101
11. Kroenke, C.D., Bretthorst, G.L., Inder, T.E., Neil, J.J.: Diffusion MR imaging characteristics of the developing primate brain. *NeuroImage* **25**(4) (May 2005) 1205–1213
12. Özcan, A.: Comparison of the complete fourier direct MRI with existing diffusion weighted MRI methods. In: *Proceedings of the 2011 IEEE International Symposium on Biomedical Imaging, Chicago, Illinois, USA (April 2011)* 931–934
13. Callaghan, P.T.: *Principles of Nuclear Magnetic Resonance Microscopy*. Oxford University Press (1991)
14. Özcan, A., Quirk, J., Wang, Y., Wang, Q., Sun, P., Spees, W., Song, S.K.: The validation of complete fourier direct mr method for diffusion mri via biological and numerical phantoms. In: *Engineering in Medicine and Biology Society, EMBC, 2011 Annual International Conference of the IEEE. (30 2011-sept. 3 2011)* 3756–3759

Appendix 3
Background and Mathematical Analysis of Diffusion MRI Methods

Background and Mathematical Analysis of Diffusion MRI Methods

Alpay Özcan,¹ Kenneth H. Wong,¹ Linda Larson-Prior,² Zang-Hee Cho,³ Seong K. Mun¹

¹ Department of Physics, Health Research, Arlington Innovation Center, Virginia Polytechnic Institute and State University, Arlington, VA 22203

² Department of Radiology, Washington University School of Medicine, St. Louis, MO 63110

³ Neuroscience Research Institute, Gachon University of Medicine and Science, Incheon, Republic of Korea 405–760

Received 24 November 2011; accepted 5 December 2011

ABSTRACT: The addition of a pair of magnetic field gradient pulses had initially enabled the measurement of spin motion to nuclear magnetic resonance (NMR) experiments. In the adaptation of diffusion weighted (DW)-NMR techniques to magnetic resonance imaging (MRI), the taxonomy of mathematical models is divided in two categories: model matching and spectral methods. In this review, the methods are summarized starting from early DW NMR models followed up with their adaptation to DW MRI. Finally, a newly introduced Fourier analysis based unifying theory, so-called Complete Fourier Direct MRI, is included to explain the mechanisms of existing methods. © 2012 Wiley Periodicals, Inc. *Int J Imaging Syst Technol*, 22, 44–52, 2012; Published online in Wiley Online Library (wileyonlinelibrary.com). DOI 10.1002/ima.22001

Key words: nuclear magnetic resonance; magnetic resonance imaging; diffusion; diffusion weighted imaging; Fourier transform

I. INTRODUCTION

Nuclear magnetic resonance (NMR) and investigation of diffusion phenomenon have led to important physical and mathematical discoveries (Mazo, et al. 2002) in the 20th century; the discovery of material properties via NMR spectroscopy and advances in the theory of stochastic processes to name two. These research areas come together in the analysis of the effect of spin diffusion on NMR signal. As the spins move in a magnetic field gradient (i.e., a changing magnetic field strength dependent on position) their magnetization vector changes individually according to their paths. This was accounted for in different manners by the pioneers of NMR: Hahn's (Hahn et al. 1950) description of diffusing spins' effects in spin echo experiment followed by Carr and Purcell's (1954) random walk approach and Torrey's incorporation of magnetization diffusion (Torrey, 1956) to Bloch equations. Torrey utilized a partial differential equation (PDE) framework instead of particle methods used by Hahn, Carr and Purcell.

In Torrey's work (1956), the effects of diffusion on NMR signal "under conditions of inhomogeneity in magnetic field" (Torrey,

1956) were mathematically formulated. Shortly thereafter, moving one step further Stejskal and Tanner intentionally introduced a pair of (homogenous) magnetic field gradients into the spin echo experiment with the purpose of accurately measuring the scalar diffusion coefficient of the sample under investigation (Stejskal and Tanner, 1965). When spins diffuse in a magnetic field gradient their transverse magnetizations disperse because the gradients or inhomogeneity creates a different magnetic field strength at each location. This changes the rotational speed of each magnetization vector according to its spin's diffusion path. Each spin possess a different path thereby creating the dispersion of the magnetization. In the particle method framework, this principle was also analyzed by McCall et al. (1963) with a statistical approach that refined Hahn's (1950) magnetization's phase distribution formulation but departing from the random walk model of Carr and Purcell (1954).

Although the pair of magnetic field gradient pulses are conventionally named as diffusion sensitizing gradients in the pulsed gradient spin echo experiment (PGSE) of Stejskal and Tanner, they do in fact encode spin motion regardless of its coherence or lack thereof (Nalcioglu and Cho, 1987). In a sense, diffusion NMR has introduced the motion information as an additional dimension before magnetic resonance imaging (MRI) increased dimensionality with addition of position of spins as an independent variable. Nevertheless, the techniques involving diffusion sensitizing gradients whether for NMR spectroscopy or MRI are called diffusion weighted (DW) methods.

Decades later, the DW technique has been adapted to MRI with great success, with early detection of ischemia (Moseley et al., 1990) being a very important example. Investigations were based on the estimation of a scalar descriptor, the so-called apparent diffusion coefficient (ADC), which represents the equivalent of isotropic diffusivity in an anisotropic environment. In other words, environments allowing unrestricted and restricted motion of molecules are compared with ADC. DW magnetic resonance (MR) measurement of anisotropy caused by three-dimensional microstructure's alteration of spin motion raised an opportunity to infer more detailed information, specifically about biological tissue. Furthermore, researchers took advantage of MRI hardware's capability of producing vectorial magnetic

Correspondence to: Alpay Özcan; e-mail: alpay@vt.edu
Grant Sponsor: US Army grant, NeuroPerformance Imaging (W23RYX1089N603)

field gradients. They developed models to express characteristics of spin motion as three dimensional constructs which traversed beyond the scalar (apparent) diffusion coefficient's potential. The most widely known of these models are perhaps the q-space formalism (Callaghan, 1991) and diffusion tensor imaging (DTI) (Basser et al., 1994; Mattiello et al., 1994). Whereas the former builds a Fourier framework between DW-MR signal and spin displacement properties, the latter projects the signal onto an ellipsoid, mathematically described by a symmetric tensor of rank two (which is a quadratic form).

These developments have pushed the initial utilization of ADC to different crucial areas in research and clinical imaging: early clinical diagnosis of ischemia (Baird and Warach, 1998), cancer diagnosis (Song et al., 2002; Xu et al., 2009) follow-up on treatment, preoperative and postoperative assessment for different organs [e.g., fiber tracking (Conturo et al., 1999; Mori and van Zijl, 2002) before brain surgery (Warfield, 2003)], monitoring of neurological diseases and disorders (Budde et al., 2008; Ciccarelli et al., 2008), neonatal development (McKinstry et al., 2002) and traumatic brain injury (Mac Donald et al., 2011). In consequence, DW-MRI is now an indispensable and versatile tool, widely used in research with an increasing number of accepted clinical applications.

II. DIFFUSION WEIGHTED MODELS FOR NMR SPECTROSCOPY

A. PDEs. The mathematical treatment of the diffusion MR signal is confined traditionally to a PDE framework, which is used for both diffusion (Crank, 1975) and Bloch equations. The starting point is Fick's first equation that describes the rate of transfer, J , of diffusing magnetization, M , through the unit area in each direction where D is the diffusion coefficient:

$$J = -D\nabla M. \quad (1)$$

Whereas Torrey (1956) leaves the scalar diffusion coefficient, D , as position dependent (thereby covering a more general case), Stejskal and Tanner (1965) following Abragam's formulation (Abragam, 1961) treat it as position independent in Fick's second equation (Crank, 1995) allowing the commutation of operators in the diffusion equation,

$$\frac{\partial M}{\partial t} = \nabla \cdot D \nabla M \rightarrow \frac{\partial M}{\partial t} = D \nabla^2 M \quad (2)$$

(t denotes time). This formulation, valid for unrestricted diffusion, as in a liquid sample, describes the Brownian motion. Accordingly, Brownian motion is mathematically modeled by Wiener process, which is defined as the stochastic process with Gaussian distributed independent increments. By this property, the Wiener process equivalently satisfies the Markovian property (Shiryayev, 1996). In other words, the spins in Brownian motion are memoryless, their future positions do not depend on their position history. On the other hand, the obstacles posed by microstructure determine the future of spin motion according to past spin interactions with microstructure. Therefore, the inclusion of Markovian property is not necessarily adequate in describing molecular motion in a restricted environment where past positions shape future motion.*

*In the investigations of microstructured environments, this is the reason the term 'apparent' appears in front of diffusion coefficient, which is defined for environments that allow unrestricted or isotropic motion.

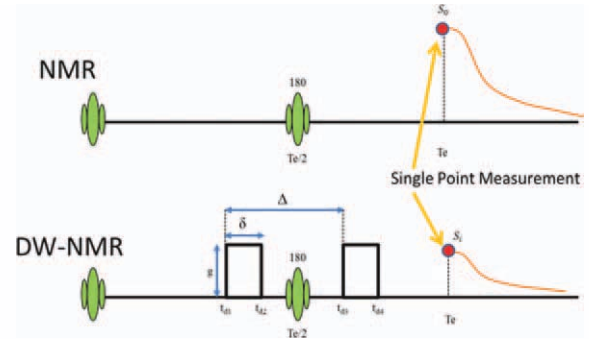


Figure 1. Spin echo (top) and pulsed gradient spin echo experiments. Diffusion sensitizing gradients are placed around the 180 degree radio frequency (RF) pulse. The duration and the separation of the pulses are δ and Δ respectively. The echo time is denoted by T_e and the measurement is the attenuation of the single point, the maximum of FID. [Color figure can be viewed in the online issue, which is available at wileyonlinelibrary.com.]

Nevertheless, the Bloch-Torrey equation, which phenomenologically describes NMR, takes this form after neglecting relaxation effects:

$$\frac{\partial M}{\partial t} = \gamma M \times B + D \nabla^2 M, \quad (3)$$

with γ and B denoting the gyromagnetic ratio and the magnetic field respectively. Proceeding with the solution of Bloch-Torrey equation for PGSE, Stejskal and Tanner rigorously obtained the characterization of the DW signal attenuation of the free induction decay's (FID) magnitude as:

$$S_i = S_0 \exp(-bD). \quad (4)$$

Here S_i denotes the magnitude of the FID corresponding to the acquisition using the i th diffusion sensitizing gradient magnitude with $i = 0$ indicating the absence of diffusion sensitizing gradients (see Fig. 1) and b is derived using the duration, Δ , the separation, Δ , times of the (rectangular) diffusion sensitizing gradients and the magnitude of the diffusion sensitizing gradient pulse g (Stejskal and Tanner, 1965):

$$b = \gamma^2 \delta^2 \left(\Delta - \frac{1}{3} \delta \right) g^2. \quad (5)$$

Basically, the attenuation is characterized as a Gaussian function of diffusion gradient strength g . The diffusion coefficient and the diffusion gradient times define the shape of the Gaussian.

B. Displacement Probabilities. Before the appearance of Torrey's PDE approach (Torrey, 1956), initial modeling of diffusion NMR in spin echo experiments by Hahn (1950) was based on the expression of the distribution of individual spins' transverse magnetization phase. Carr and Purcell (1954) interpreted diffusion using a random walk model to arrive at Hahn's result for signal attenuation:

$$S_i = S_0 \exp\left(-\frac{2}{3} \gamma^2 g^2 T_e^3 D\right). \quad (6)$$

Unlike in the case of PGSE experiment, g represents here a constant magnetic field gradient rather than the strength of pulsed gradients of Figure 1.

Around the publication time of Stejskal and Tanner’s seminal work (Stejskal and Tanner, 1965), another less noticed work treating diffusion NMR signal via particle methods was published by McCall et al. (1963). The work departed from the random walk formulation of Carr and Purcell (1954), which records the phase of the transverse magnetization during each random walk step in a magnetic field gradient. The analysis of McCall et al. (1963) returned to the initial statistical treatment of Hahn (1950) describing the magnetization phase distribution caused by spin motion. Despite minor mathematical discrepancies,[†] the fruitful idea refines Hahn’s (1950) analysis by expressing the individual phase directly as a function of spin displacements and obtains exactly Eq. (6).

More than two decades after the publication of McCall et al. (1963), Callaghan modeled the PGSE signal using techniques of scattering theory in the spirit of particle methods. In the model, an analogy between the probability of “finding any scattering center” (Callaghan, 1991) and the probability of spin displacements creates the so-called q-space model. With the narrow pulse assumption, i.e., negligible diffusion gradient pulse duration in comparison with the separation time, $\delta \ll \Delta$, Callaghan computes the amplitude of the echo at T_e as

$$E(G_D) = \int \rho(x) \int P_s(x', \Delta|x) \exp(i\gamma\delta G_D \cdot (x' - x)) dx' dx \quad (7)$$

with ρ and G_D denoting the spin density and the three dimensional diffusion sensitizing magnetic field gradient vector respectively. P_s is the probability of a particle initially at x to be found at x' after the pulse separation time, Δ . Relying on Markovian property, Callaghan rewrites Eq. (7) using the “dynamic displacement”: $R = x' - x$, and the average propagator (Callaghan, 1991), $\bar{P}(R, \Delta)$, which “gives the average probability for any particle to have a dynamic displacement R over a time Δ ” (Callaghan, 1991). Accordingly the signal at echo time is calculated as:

$$E(q) = \int \bar{P}(R, \Delta) \exp(i2\pi q \cdot R) dR, \quad (8)$$

where $q = (2\pi)^{-1}\gamma\delta G$, giving the name q-space.

The derivations of these results are strongly dependent on the single point measurements at echo time (see Fig. 1). However, the same reasoning is not applicable to DW-MRI for the reasons that will be explained in Section 4.

Finally, it is worth pointing out that particle methods and PDE’s are equivalent mathematically (Feller, 1967). Consequently, both PDE and particle methods based derivations are valid for DW methods.

III. DW MRI MODELS

In comparison with NMR spectroscopy, MRI scanner hardware creates three dimensional magnetic field gradients that allow the measurement of spin density as a function of position. The spin density, usually weighted by relaxation times (T_1 , T_2) is presented as an image. In other words, as an improvement to obtaining an average measurement from the whole sample of NMR spectroscopy, MRI augments the signal dimensionality by adding positional informa-

[†]The assertion that the integrals of sample paths of a Gaussian distributed stochastic process are Gaussian does not exist in the reference provided in the manuscript (Munroe, 1951.). In fact, its proof does not exist in the literature to the best of the authors’ knowledge.

tion. Beginning in the late 1980s, diffusion methods were adapted to MRI using the mathematical models of DW-NMR described in Sections II.A. and II.B. An important leap occurred when researchers moved from the investigations of the scalar quantity (ADC) to the estimation of more general three dimensional geometric constructs. For example, DTI estimates ellipsoids defined by a quadratic form (diffusion tensor), D , which is basically a symmetric 3×3 matrix. The scalar quantity ADC is equal to the mean of the eigenvalues of the matrix D .

DW-MRI methods can be grouped under two general categories:

1. **Model Matching Methods** initiated by DTI (Basser et al., 1994; Matiello et al., 1994) and refined with high angular resolution diffusion-weighted imaging (HARDI) (Frank, 2001), composite hindered and restricted model of diffusion (CHARMED) (Assaf and Basser, 2005), spherical deconvolution (Tournier et al., 2004), diffusion orientation transform (DOT) (Ozarslan et al., 2006) two versions of the generalized DTI (GDTI) (Özarslan and Mareci, 2003; Liu et al., 2004) and diffusional kurtosis imaging (DKI) (Jensen et al., 2005).
2. **Spectral methods** originating from Callaghan’s q-space (Callaghan, 1991) followed by the diffusion spectrum imaging (DSI) (Wedeen et al., 2005), Q-ball imaging (QBI) (Tuch et al., 2003).

A. Model Matching Methods. DW-MRI model matching methods are direct adaptations of signal attenuation modeling in DW-NMR spectroscopy. The models assume that images obtained with diffusion sensitizing gradients demonstrate different attenuation levels at different pixels as a function of diffusion gradient vectors. This reflects characteristics of spin motion dictated by the microstructure. The model matching method is described by the following generic equation adopted from Eq. (4):

$$I_i = I_0 \exp(-H(G_{Di})). \quad (9)$$

Here, the model is no longer for the FID but its Fourier transform, which is in the image domain: I_i is the intensity (magnitude in most cases) of a given pixel from the image obtained with the i th diffusion gradient vector G_{Di} . The methods are defined by the functional presentation of the model, H . The data are projected onto H , which also incorporates the unknown to be estimated, namely the spin motion descriptor.

A.1. DTI. In the original formulation of model matching pioneering work, DTI (Basser et al., 1994; Matiello et al., 1994), the function is

$$H = B(G_{Di}, \delta, \Delta) : D. \quad (10)$$

The descriptor is the diffusion tensor D to be estimated from the (now 3 dimensional) Bloch-Torrey equation [Eq. (3)]. B is a matrix valued function of G_{Di} , δ , Δ (Matiello et al., 1994) and it multiplies D element-by-element. This formulation is refined to a natural linear algebraic framework by Papadakis et al. (1999) who noticed that in fact

$$B(G_{Di}, \delta, \Delta) : D = \gamma^2 b_t G_{Di}^T D G_{Di}. \quad (11)$$

The constant coefficient $b_t = \delta^2(\Delta - \frac{1}{3}\delta)$, introduced later in (Özcan, 2005) delineates the gradient duration and separation times

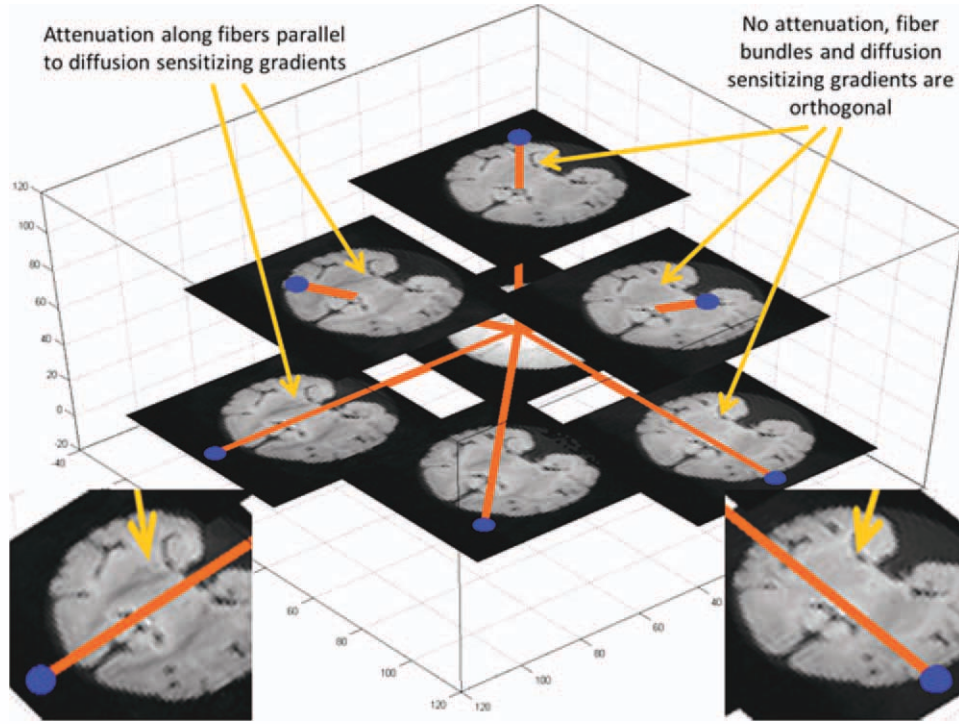


Figure 2. DW images from a PGSE experiment of an ex-vivo baboon brain (Özcan 2010; Özcan, 2011) shown on top of the diffusion sensitizing gradient vectors (orange vectors with blue ends) of the DGS. The image at the origin is acquired without diffusion gradients and therefore is unattenuated. The attenuation is highest on the fibers parallel to the diffusion gradient vector as shown in two zoomed images on the left and right bottom. [Color figure can be viewed in the online issue, which is available at wileyonlinelibrary.com.]

(δ , Δ) from their vector part G_{D_i} in contrast to b of Eq. (5). Conventional diffusion gradient schemes (DGS, the list of diffusion sensitizing gradient vectors used in a DW experiment) are specified using a single b -value for the entire diffusion gradient vectors G_{D_i} thereby confining all of them onto a sphere. The introduction of b_i made possible the design of new DGS via optimization methods. In (Özcan, 2011), the effect of imaging gradients is minimized with DGSs containing vectors of different magnitudes optimally placed with respect to the imaging magnetic field gradients.

At a basic level, Eq. (11) implies that D estimated from DTI experiments is forcefully a symmetric matrix because for any vector G , $G^T D G = G^T D^T G$ and

$$2G^T D G = G^T (D + D^T) G + G^T (D - D^T) G = G^T (D + D^T) G. \quad (12)$$

In other words, DTI can only measure the symmetric part of the diffusion tensor: $\frac{1}{2}(D + D^T)$. Symmetric matrices form a subspace and 3×3 symmetric matrices are represented as six dimensional vectors, $d = [d_1, d_2, d_3, d_4, d_5, d_6]$:

$$D = \begin{bmatrix} d_1 & d_4 & d_6 \\ d_4 & d_2 & d_5 \\ d_6 & d_5 & d_3 \end{bmatrix}. \quad (13)$$

This allows rewriting Eq. (11) in a linear form following the steps of Papadakis et al. (1999) and the refinements in (Özcan, 2005):

$$\gamma^2 b_i G_{D_i}^T D G_{D_i} = \gamma^2 b_i v_i d \quad (14)$$

with

$$v_i = [g_{ix}^2, g_{iy}^2, g_{iz}^2, 2g_{ix}g_{iy}, 2g_{iy}g_{iz}, 2g_{ix}g_{iz}] \quad (15)$$

where $G_{D_i} = [g_{ix}, g_{iy}, g_{iz}]$.

To solve for six elements of d , a minimum of six DW images plus one unattenuated image, I_0 , are acquired, $m \geq 6$ (see Fig. 2) and the logarithm of Eq. (9) is taken to give a set of linear equations:

$$\gamma^2 b_i V_g d = \gamma^2 b_i \begin{bmatrix} v_1 \\ \vdots \\ v_m \end{bmatrix} d = \begin{bmatrix} \ln(I_0) - \ln(I_1) \\ \vdots \\ \ln(I_0) - \ln(I_m) \end{bmatrix}. \quad (16)$$

The list of the gradient vectors used for the acquisition of DW images is called the DGS (Özcan, 2010a, 2010b, 2011). An example of DGS with the corresponding images is shown in Figure 2. It follows from elementary linear algebra that for Eq. (16) to have a

unique solution, the coefficient matrix, $V_g = \begin{bmatrix} v_1 \\ \vdots \\ v_m \end{bmatrix}$, must have full

rank. V_g is a function of DGS vectors [see Eq. (15)] and therefore the vectors must be chosen appropriately to guarantee the uniqueness of the solution. A set of mathematical necessary conditions for the choice of diffusion gradients that would guarantee the full rank condition were given in (Özcan, 2005) a decade after the introduction of DTI.

Once the solution for d is found, the symmetric matrix D is reconstructed as in Eq. (13) at each pixel. A standard theorem in

linear algebra proves that symmetric matrices, thus the diffusion tensor, have orthogonal eigenvectors and real eigenvalues ($\lambda_1 \geq \lambda_2 \geq \lambda_3$). The setup is general in the sense that ADC can be calculated as the mean of the eigenvalues.

In this three-dimensional structure, whereas the eigenvectors indicate the principal directions of the motion, corresponding eigenvalues describe the tendency of the spins to move in each direction. If all the eigenvalues are equal, the medium is isotropic as in a liquid. However, if the microstructure favors motion in a given direction, causing anisotropy, the eigenvalues will reflect that by differing from each other. Functions of the three eigenvalues describing their dispersion are called anisotropy measures, fractional anisotropy being one of the most used ones (Basser and Pierpaoli, 1996):

$$FA = \frac{\sqrt{(\lambda_1 - \lambda_2)^2 + (\lambda_2 - \lambda_3)^2 + (\lambda_3 - \lambda_1)^2}}{\sqrt{2(\lambda_1^2 + \lambda_2^2 + \lambda_3^2)}}. \quad (17)$$

Usually, an anisotropy map describing the microstructure is shown as an image with the value of anisotropy index at each pixel. The directional information might be added by displaying the eigenvector corresponding to the largest eigenvalue at each pixel as a ‘‘whisker’’ (thus the name whisker plot). The directionality is also shown with a color image. A different color channel is assigned to each direction to display three components of the eigenvector accordingly. There are different applicable schemes depending on the properties of the spin motion (Pajevic and Pierpaoli, 1999). The combined directional and motion tendency can also be shown by overlaying ellipsoids defined by the diffusion tensor ($x^T D x = \text{constant}$) on each pixel of an anatomic image. The equation of an ellipse requires that the eigenvalues of D are all greater than or equal to 0. Otherwise, the diffusion equation, Eq. (2), contradicts the conservation of mass. This physical constraint is sometimes violated in the estimation obtained from experimental DTI data. The reasons for the occurrences of negative eigenvalues from experimental data constitute currently an open question.

B. High Order Model Matching Methods. DTI can be considered as a second order approximation to the attenuation function H of Eq. (9). Different expansions of the attenuation function result in different model matching methods. In HARDI (Frank, 2001), the attenuation is expanded using the spherical harmonics Y_l^m (Frank, 2001)

$$H(G_{Di}(\theta, \varphi)) = \sum_{l=0}^{\infty} \sum_{m=-l}^l a_{lm} Y_l^m(\theta, \varphi) \quad (18)$$

where (θ, φ) are the azimuthal and polar angles in the spherical coordinates. The coefficients, a_{lm} , are computed from Eq. (18) using the experimental data. The odd numbered harmonics $l = 1, 3, 5, \dots$ are discarded on the basis that they are asymmetric (Frank, 2001).

A generalization of HARDI is provided by Tournier et al. (2004) in spherical deconvolution, utilizing concepts from linear systems theory with the use of a response function (also known as point spread function or transfer function in control theory) in spherical coordinates. The response function, equivalent to impulse response of a linear time invariant dynamical system, describes the signal originating from a single nerve fiber. To assess the distribution of multiple fibers within a voxel, the full set of measurements is deconvolved with the response function. The result is the fiber orientation density function.

In DKI (Jensen et al., 2005), a higher order expansion using the concept of excess kurtosis is implemented. H is expanded by adding the kurtosis tensor to the diffusion tensor D (Jensen et al., 2005):

$$H(G_{Di}) = \gamma^2 b_i G_{Di}^T D G_{Di} - \frac{ADC}{6} \gamma^4 b_i^2 D^{(4)}(G_{Di}, G_{Di}, G_{Di}, G_{Di}). \quad (19)$$

The kurtosis tensor $D^{(4)}$ is a symmetric tensor of rank 4 and the method is a generalization of DTI.[‡] The expansion strategy of Eq. (19) appeared before the work of Jensen et al. (2005). Özarslan and Mareci (2003) integrated higher rank tensors into the Bloch-Torrey equations. The odd ranked tensor elements result in negative diffusion coefficients (Özarslan and Mareci, 2003). Özarslan and Mareci (2003) argue that ‘‘since negative diffusion coefficients are non-physical, the rank is forced to be an even number’’ (see also the discussion about the negative eigenvalues in Section III.A.1.). Consequently, the generalized diffusion tensor (GDT) approximation of H is given as:

$$H(G_{Di}) = \gamma^2 b_i \sum_{n=1}^{\infty} D^{(2n)}, \quad (20)$$

The n arguments each of $D^{(n)}$ operates on is G_{Di} , e.g., in the last term of Eq. (19) where $n = 4$. About a year after the publication of (Özarslan and Mareci, 2003), Liu et al. (2004) published another GDT imaging model that incorporates higher order tensors of all ranks:

$$H(G_{Di}) = \sum_{n=2}^{\infty} j^n \gamma^{2n} b_i^{(n)} D^{(n)}, \quad (21)$$

where $j = \sqrt{-1}$ and $b_i^{(n)}$'s are higher order integrals of the diffusion sensitizing gradient's time course. The inclusion of higher rank tensors is made possible by allowing the signal to be complex valued. In Eq. (19), odd ranked tensors form the imaginary part of the signal. In addition, they are asymmetric terms and this covers physically a more general situation.

The general aim of these model matching methods is to estimate the descriptors of diffusion that would minimize the model matching error originating from the measurement values, $\hat{I}_1, \dots, \hat{I}_m$:

$$\left\| \begin{bmatrix} \hat{I}_1 \\ \vdots \\ \hat{I}_m \end{bmatrix} - I_0 \begin{bmatrix} \exp(-H(G_{D1})) \\ \vdots \\ \exp(-H(G_{Dm})) \end{bmatrix} \right\|. \quad (22)$$

The solution of the minimization problem of Eq. (22) for each model matching method results in the determination of a number of unknowns (e.g., 6 for DTI) specified by the model equations presented in this section. Naturally this number is also the minimum number of diffusion gradient vectors in DGS. Furthermore, in a parallel observation to the DTI estimation equations, the conditions on DGS guaranteeing the uniqueness of solution for different model matching methods have not been investigated and remain as an open and untouched subject of discussion.

[‡]For example, D is a rank two tensor and both of its arguments are equal to G_{Di} . Therefore, it is a quadratic form that can be represented as a matrix. Its value at G_{Di} is found by left and right vector-matrix multiplication i.e., $D(G_{Di}, G_{Di}) = G_{Di}^T D G_{Di}$. Higher rank tensors have more complicated representations than vector-matrix multiplication.

In addition to the aforementioned methods that are using the attenuation model of Eq. (9), there are two techniques that are compartmentalizing and approximating the q-space signal of Section II.B. The first one, composite hindered and restricted model of diffusion (CHARMED) (Assaf and Basser, 2005), divides the signal into two compartments as ‘‘hindered water diffusion in the extra-axonal space and restricted water diffusion in the intra-axonal space.’’ Accordingly the q-space signal originating from multiple compartments at the echo time is given as

$$E(q) = \sum_{i=1}^L f_h^i S_h^i + \sum_{j=1}^N f_r^j S_r^j \quad (23)$$

where ‘‘ L is the number of distinct hindered compartments and N is the number of distinct restricted components’’ (Assaf and Basser, 2005), f_h and f_r^j are volume fractions of the compartments. Each of the compartments are further dissected to divide the signal into parallel and perpendicular (e.g., to axons) sections to obtain a final model. The second technique, DOT of Özarlan et al. (2006), takes the different path of expanding theoretically the Fourier Transform in Eq. (9) using spherical harmonics. The propagator, \bar{P} of Eq. (8), is expressed in the basis formed by the spherical harmonics. The expression, in essence, is the same as Eq. (18) but it is the propagator, rather than the attenuation, that is approximated.

C. Spectral Methods. The basis of the spectral methods for DW-MRI is the adaptation of NMR q-space equation, Eq. (8), to MRI. (Callaghan, 1991):

$$S(k, q) = \int \rho(x) E(q) \exp(i2\pi k \cdot x) dx, \quad (24)$$

where k is the usual MRI k-space variable and $E(q)$ is the adaptation of its NMR definition in Eq. (7)

$$E(q) = \int P_s(x', \Delta|x) \exp(i\gamma\delta G_D \cdot (x' - x)) dx'. \quad (25)$$

Clearly, in this equation, $E(q)$ is a function of position x . Accordingly, it must be taken into account for the evaluation of the integral in Eq. (24). To obtain Eq. (24), on p. 440 of (Callaghan, 1991) it is asserted that ‘‘despite the fact that both P_s and ρ may depend on x , the effect of the PGSE sequence is quite separable. . .’’. It is also indicated that the signal comes from the finite volume element corresponding to the imaging voxel. In consequence, $E(q)$ should be seen as ‘‘the Fourier transform of local dynamic profile’’ according to Eq. (8.7), p. 440, (Callaghan, 1991):

$$E(q) = \int \bar{P}(R, \Delta) \exp(i2\pi q \cdot R) dR. \quad (26)$$

The goal of the method is the reconstruction of the average propagator using the Fourier transform from the measurements after their normalization. This is explicitly formulized in diffusion spectrum imaging (DSI) method of Wedeen [Eq. (4), (Wedeen et al., 2005):

$$\bar{P}(R, \Delta) = I_0^{-1} (2\pi)^{-3} \int |I(q)| \exp(-2i\pi q \cdot R) dq. \quad (27)$$

Here, $I(q)$ is the (complex) pixel intensity corresponding to diffusion sensitizing gradient that produces q . In other words, $I(q) = I_i$

which is the image obtained with G_{Di} such that $q = (2\pi)^{-1} \gamma \delta G_{Di}$. The magnitude is taken ‘‘to exclude phase shifts arising from tissue motion’’ (paragraph preceding Eq. (4), (Wedeen et al., 2005)). In DSI the main interest is the angular structure of the diffusion spectrum. The final product is the orientation distribution function defined as ‘a weighted radial summation of $\bar{P}(R, \Delta)$ ’ (Wedeen et al., 2005):

$$ODF(u) = \int \bar{P}(ru, \Delta) r^2 dr \quad \text{with } \|u\| = 1 \text{ for } r > 0. \quad (28)$$

It is important to note the derivations in (Wedeen et al., 2005) rely on Markovian property and the narrow pulse approximation. Moreover, the magnitude of the signal is used on the basis that ‘‘the MRI signal is positive for any type of spin motion without net flux’’ (Wedeen et al., 2005). Under these assumptions, the model is not completely unconstrained.

The Fourier reconstruction in general requires a large number of DW acquisitions compared with model matching methods. In DSI, the sampling of q-space is realized within a sphere. The issue of large number of acquisition is addressed by the use of the so-called QBI technique (Tuch et al., 2003). As in DSI, in QBI the quantity of interest is the orientation distribution function which is defined slightly different than DSI-ODF:

$$\psi(u) = \int \bar{P}(ru, \Delta) dr \quad \text{with } \|u\| = 1 \text{ for } r > 0. \quad (29)$$

By utilizing of the Funk-Radon transform, QBI estimates ψ with measurements obtained on a ball (hence the method’s name, QBI) in q-space, with significantly smaller number of acquisitions.

IV. A HIGHER DIMENSIONAL FOURIER RELATIONSHIP

The methods described in previous sections are just representatives of many existing variations of DW-MR methods and techniques that were not listed here due to space restrictions. An exhaustive list can be found in the publication by Jian et al. (2007). The sheer number of methods could be considered as an indication of dissatisfaction with the performance of existing methods, especially originating from inadequacies that arise when identification of the microstructure of geometrically complex regions (e.g., fiber tract crossings) is attempted. One reason behind the inadequacy is the creation of DW-MRI models of Section III by direct adoption of DW-NMR models.

The following important considerations arise in the course of the adoption:

1. In contrast to DW-NMR, in MRI the signal does *not* originate from a single point at echo time (see Section II). Even in MRI without diffusion weighting, all of the points in FID fill up the k -space and therefore all of them are necessary to construct the image or the volume.
2. Imaging gradients, which are naturally absent in NMR, are usually ignored in DW-MRI models. Attempts to integrate imaging gradient effects have unveiled significant problems in the derivation of DTI model (Özcan, 2010a). Moreover, these problems cannot be remedied neither with optimization (Özcan, 2011) nor with nonlinear estimation (Özcan, 2010b).
3. With the exception of Torrey’s approach (Torrey, 1956), D is treated as a position independent quantity within all of the models. For example, DTI relies on the assumption that ‘‘the

diffusion coefficients are independent of space (position) within a voxel” [p. 253, (Basser et al., 1994)]. Otherwise, DTI estimation equations cannot be derived. Position dependence complicates severely the solution of PDEs for DW imaging models.

4. The narrow pulse approximation is unrealistic. Considering that Wiener process has nondifferentiable continuous sample paths, the irregularities of the spin motion are at a level of complexity which is unresolvable at any time scale regardless how short are the duration of the pulses.
5. With the exception of GDTI proposed by Liu et al. (2004), the models obtain symmetric quantities either by projecting the data onto symmetric constructs (e.g., ellipsoids of DTI), pruning the asymmetric structures (see Section III.B. with spherical harmonics of HARDI or odd ranked tensors of DOT) or by using the magnitude of the signal in spectral methods which forces the Fourier transform to result in (Hermitian) symmetric outcomes. An appropriate model must be unconstrained so that any property such as symmetry should be revealed by the data themselves establishing an evidence based methodology. Modeling presumptions constrain the outcome of the investigations.
6. Models rely on Markovian property which is not justifiable in restricted environments such as biological tissue (see Section II.A.).

Motivated by these concerns, a new accurate and unifying Fourier-based theory of DW-MRI has been developed by returning to the first principles of DW-MR signal formation in (Özcan, 2010c; Özcan, 2011; Özcan et al., 2011). The DW-MRI signal is modeled by expressing the evolution of the phase (Ω_i) of the i th spin’s transverse magnetization,

$$m_i(t) = \exp(-j\gamma\Omega_i)m_i(t_0) \quad (30)$$

Eq. (30) is the Bloch equation obtained when relaxations are neglected. The magnetization changes according to the displacement w_i from the initial position $x_i(t_0)$:

$$x_i(t) = x_i(t_0) + w_i(t), \quad (31)$$

because of the diffusion sensitizing magnetic field gradients (see Section I). When the signal formation is derived for the PGSE experiment (Özcan, 2010c) using Eq. (32) and (33), the initial position $x_i(t_0)$ and the i th spin’s displacement integral, W_i^d ,

$$W_i^d = \int_{t_{d1}}^{t_{d2}} w_i(\tau)d\tau - \int_{t_{d3}}^{t_{d4}} w_i(\tau)d\tau, \quad (32)$$

(see Fig. 1 for the definition of t_{di}) appear in the formulations. Furthermore, the derivations in (Özcan, 2010c) show that the complex valued DW-MRI signal that comes out of the MR scanner is the Fourier transform of the joint distribution of the number of spins starting from the initial position x and possessing W^d displacement integrals: $P_{\text{cfid}}(x, W^d)$:

$$S_{\text{cfid}}(k_{\text{mr}}, k_{\text{D}}) = \mathbf{F}[P_{\text{cfid}}(x, W^d)] \quad (33)$$

Accordingly, the method is named complete Fourier direct (CFD) MRI because the entire (complex valued) data constitute the Fourier transform of the distribution function $P_{\text{cfid}}(x, W^d)$. In Eq. (33), the

Fourier variables k_{mr} and k_{D} are the usual MR imaging k-space variable (read-out and slice select) and the diffusion sensitizing gradient vector $k_{\text{D}} = G_{\text{D}}$ respectively. Basically, CFD-MRI augments the dimension of MR imaging by adding, on top of position information of MRI (see also the discussion on paragraph 3 in Section I), three more dimensions corresponding to displacement integrals. In contrast to the existing methods, the unifying CFD-MR framework does not separate position and displacement portions. In fact, in the derivations of CFD model, $P_{\text{cfid}}(x, W^d)$ comes up naturally as a joint distribution function.

It is very important to note that Eq. (33) is the final product of intermediate steps that guarantee the preservation of S_{cfid} ’s Hermitian symmetry (Özcan, 2010c). This property is the only physical evidence at hand because the only known fact is that P_{cfid} is a real valued function being the count of (large but) finite number of spins. This implies that its Fourier transform in Eq. (33) must be Hermitian,

$$S_{\text{cfid}}(k_{\text{mr}}, k_{\text{D}}) = S_{\text{cfid}}^*(-k_{\text{mr}}, -k_{\text{D}}) \quad (34)$$

(* denotes the complex conjugation).

P_{cfid} is reconstructed by taking the inverse Fourier transform of the entire data:

$$P_{\text{cfid}}(x, W^d) = \mathbf{F}^{-1}[S_{\text{cfid}}(k_{\text{mr}}, k_{\text{D}})]. \quad (35)$$

CFD-MRI addresses the concerns raised in the beginning of this section as follows:

1. CFD-MRI calculations incorporate all of the data. The signal is not calculated from a single point but from all the points of augmented CFD k-space defined by $k_{\text{CFD}} = (k_{\text{mr}}, k_{\text{D}})$. k_{CFD} is either 5 or 6 dimensional depending on whether slice or volume imaging is conducted. The last 3 dimensions come from 3 dimensional displacement integral vectors defined in Eq. (32).
2. Imaging gradients are included by means of k_{mr} .
3. CFD-MRI expresses position dependence inherently in the first argument of joint distribution function $P_{\text{cfid}}(x, W^d)$ which is the initial position.
4. There is no need for the narrow pulse assumption. In Eq. (32), the integrals are evaluated during the diffusion sensitizing gradient times.
5. The signal is treated as a complex valued quantity in contrast to using the magnitude. By preserving the Hermitian symmetry during the evaluation of Eq. (35), asymmetry is allowed in $P_{\text{cfid}}(x, W^d)$. This guarantees an evidence based approach: if there is asymmetry or symmetry in the motion characteristics, data will show it.
6. The only assumption in Eq. (31) is the continuity of the displacement w_i since a spin cannot disappear at one point and reappear at a different one. In addition, the displacement integral, W^d , is not a stochastic processes. Therefore any property thereof, such as being Markovian, is not needed to be in the model. Accordingly, CFD-MRI points out that the propagator is *not* the quantity that is being measured.

The simplicity of Eq. (30) (Bloch equation) and Eq. (31) (the most general equation of motion) make their combination tractable by use of particle methods. CFD-MRI model would be hard to

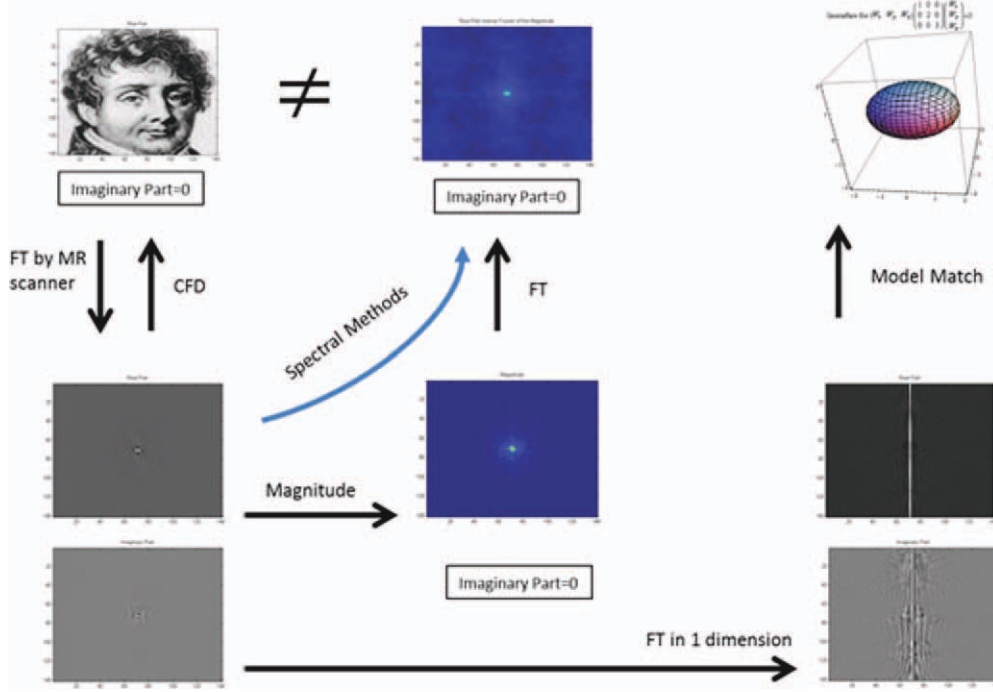


Figure 3. The summary of the DW methods is shown using the Fourier transform of Fourier's portrait on top right corner. MR scanner takes the full Fourier transform of the portrait. CFD-MRI reconstructs the portrait by using the inverse transform. Spectral methods take the magnitude of the transform and compute the inverse transform. The outcome, shown in the middle column on top, does not resemble the original portrait. Model matching methods (arrow at the bottom) evaluate the inverse transform in imaging domain and work in a mixed physical-frequency space. [Color figure can be viewed in the online issue, which is available at wileyonlinelibrary.com.]

derive using a PDE framework. However, theoretical equivalence of the two methods (Feller, 1967) indicates that particle method derivations are sufficient for modeling.

The Fourier relationship established with CFD-MRI clarifies the mechanisms of existing methods. For example, the Wiener process that describes self-diffusion in a liquid has displacements, w_i , that are Gaussian distributed with 0 mean and covariance matrix equal to the diffusion tensor D . It can be derived after tedious but routine calculations that the displacement integrals, W_i^d , have mean equal to 0 and covariance equal to (Özcan, 2011)

$$E[W_i^d(W_i^d)^T] = \delta^2 \left(\Delta - \frac{1}{3} \delta \right) D = b_i D. \quad (36)$$

This equation shows that the MR scanner acts as a filter on the diffusion process by scaling its covariance with b_i that only depends the duration and separation times of the diffusion sensitizing gradients. The DW signal that comes out of the scanner is the Fourier transform of the distribution.

Gaussians are eigenfunctions of the Fourier transform, i.e. the Fourier transform of a Gaussian is also a Gaussian (Özcan, 2011):

$$\mathbf{F} \left[\exp((W_i^d)^T (b_i D)^{-1} W_i^d) \right] \cong \exp((k_D)^T (b_i D) k_D). \quad (37)$$

Equation (37) is key in understanding the model matching methods. Equation (9) is obtained by evaluating the Fourier transform in half of the variables, namely the imaging portion defined by k_{mr} and leaving the displacement integral portion k_D intact. In this mixed physical-frequency variable setup, the displacement portion remains on the Fourier domain. According to the right hand side of Eq. (37), DTI estimates D

in Fourier domain more easily than in the physical domain on the left side which involves of the inverse of D . In more complex microstructures, high order approximations follow the same strategy. They attempt to expand the mathematical Fourier transform by adding higher order terms described in Section 9 to the argument of the eigenfunction.

According to Eq. (35), CFD-MRI reconstructs P_{cfid} using the inverse Fourier transform (discrete Fourier transform is used in practice). Spectral methods of Section IV are based on the same principle but CFD evaluates the Fourier transform correctly (see item 5 above), i.e., using complex valued signals. It obtains the correct distribution function (see item 6 above), in the sense that P_{cfid} being a joint distribution, cannot necessarily be factored into a spin density and displacement descriptor. The mechanisms behind the methods are summarized in Figure 3.

V. CONCLUSIONS

All DW-MRI models process the data with the same goal in mind: noninvasive description of microstructural changes that will endow extraction of relevant information pertaining to diagnosis, prognosis and management of important health problems from different areas. The large number of models described herein is proof of continuing research effort in the quest of a more adequate model for DW-MRI. The unification of the plethora of approaches will improve the accuracy of the assessment provided by the modality. In this manuscript, the methods are summarized by describing their mathematical properties. In addition, they are interpreted using the Fourier based CFD-MRI method with the aim of reaching a consensus among the methods. An important goal is the incorporation of these new findings into the tractography methods, which is reserved for future studies.

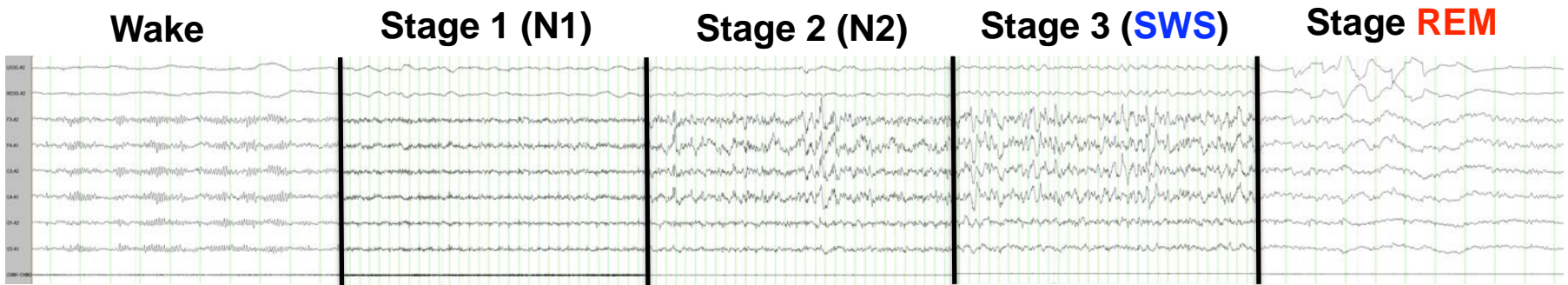
REFERENCES

- A. Abragam, *The principles of nuclear magnetism*, Clarendon Press, Oxford, 1961.
- Y. Assaf and P. Basser, Composite hindered and restricted model of diffusion (charmed) mr imaging of the human brain, *Neuroimage* 27 (2005), 48–58.
- A.E. Baird and S. Warach, Magnetic resonance imaging of acute stroke, *J Cereb Blood Flow Metab* 18 (1998), 583–609.
- P.J. Basser and C. Pierpaoli, Microstructural and physiological features of tissues elucidated by quantitative-diffusion-tensor MRI, *J Magn Reson B* 111 (1996), 209–219.
- P.J. Basser, J. Mattiello, and D. LeBihan, Estimation of the effective self-diffusion tensor from the NMR spin echo, *J Magn Reson B* 103 (1994), 247–254.
- M.D. Budde, J.H. Kim, H.F. Liang, J.H. Russell, A.H. Cross, and S.K. Song, Axonal injury detected by in vivo diffusion tensor imaging correlates with neurological disability in a mouse model of multiple sclerosis, *NMR Biomed* 21 (2008), 589–597.
- P.T. Callaghan, *Principles of nuclear magnetic resonance microscopy*, Oxford University Press, Oxford [England] New York, 1991.
- H.Y. Carr and E.M. Purcell, Effects of diffusion on free precession in nuclear magnetic resonance experiments, *Phys Rev* 94 (1954), 630–638.
- O. Ciccarelli, M. Catani, H. Johansen-Berg, C. Clark, and A. Thompson, Diffusion-based tractography in neurological disorders: Concepts, applications, and future developments, *Lancet Neurol* 7 (2008), 715–727.
- T.E. Conturo, N.F. Lori, T.S. Cull, E. Akbudak, A.Z. Snyder, J.S. Shimony, R.C. McKinstry, H. Burton, and M.E. Raichle, Tracking neuronal fiber pathways in the living human brain, *Proc Natl Acad Sci U S A* 96 (1999), 10422–10427.
- J. Crank, *The mathematics of diffusion*, Oxford University Press, United States, 1975.
- W. Feller, *An introduction to probability theory and its applications*, Wiley, New York, 1967.
- L.R. Frank, Anisotropy in high angular resolution diffusion-weighted MRI, *Magn Reson Med* 45 (2001), 935–939.
- E.L. Hahn, Spin echoes, *Physical Rev* 80 (1950), 580–594.
- J.H. Jensen, J.A. Helpert, A. Ramani, H. Lu, and K. Kaczynski, Diffusional kurtosis imaging: The quantification of non-gaussian water diffusion by means of magnetic resonance imaging, *Magn Reson Med* 53 (2005), 1432–1440.
- B. Jian, B.C. Vemuri, E. Ozarslan, P.R. Carney, and T.H. Mareci, A novel tensor distribution model for the diffusion-weighted MR signal, *Neuroimage* 37 (2007), 164–176.
- C. Liu, R. Bammer, B. Acar, and M.E. Moseley, Characterizing non-gaussian diffusion by using generalized diffusion tensors, *Magn Reson Med* 51 (2004), 924–937.
- C.L. Mac Donald, A.M. Johnson, D. Cooper, E.C. Nelson, N.J. Werner, J.S. Shimony, A.Z. Snyder, M.E. Raichle, J.R. Witherow, R. Fang, S.F. Flaherty, and D.L. Brody, Detection of blast-related traumatic brain injury in u.S. Military personnel, *N Engl J Med* 364 (2011), 2091–2100.
- J. Mattiello, P.J. Basser, and D. LeBihan, Analytical expressions for the b matrix in NMR diffusion imaging and spectroscopy, *J Magn Reson Ser A* 108 (1994), 131–141.
- R.M. Mazo, *Brownian motion: Fluctuations, dynamics, and applications*, Oxford University Press, USA, 2002.
- D.W. McCall, D.C. Douglass, and E.W. Anderson, Self-diffusion studies by means of nuclear magnetic resonance spin-echo techniques, *Berichte der Bunsengesellschaft für Physikalische Chemie* 67 (1963), 336–340.
- R.C. McKinstry, A. Mathur, J.H. Miller, A. Ozcan, A.Z. Snyder, G.L. Scheffert, C.R. Almlil, S.I. Shiran, T.E. Conturo, and J.J. Neil, Radial organization of developing preterm human cerebral cortex revealed by non-invasive water diffusion anisotropy MRI, *Cereb Cortex* 12 (2002), 1237–1243.
- S. Mori and P.C. van Zijl, Fiber tracking: Principles and strategies - a technical review, *NMR Biomed* 15 (2002), 468–480.
- M.E. Moseley, Y. Cohen, J. Mintorovitch, L. Chileuit, H. Shimizu, J. Kucharczyk, M.F. Wendland, and P.R. Weinstein, Early detection of regional cerebral ischemia in cats: Comparison of diffusion- and t2-weighted MRI and spectroscopy, *Magn Reson Med* 14 (1990), 330–346.
- M.E. Munroe, *Theory of probability*, McGraw-Hill, New York, 1951.
- O. Nalcioglu and Z.H. Cho, Measurement of bulk and random directional velocity fields by NMR imaging, *IEEE Trans Med Imaging* 6 (1987), 356–359.
- E. Özarslan and T.H. Mareci, Generalized diffusion tensor imaging and analytical relationships between diffusion tensor imaging and high angular resolution diffusion imaging, *Magn Reson Med* 50 (2003), 955–965.
- E. Ozarslan, T.M. Shepherd, B.C. Vemuri, S.J. Blackband, and T.H. Mareci, Resolution of complex tissue microarchitecture using the diffusion orientation transform (DOT), *Neuroimage* 31 (2006), 1086–1103.
- A. Özcan, (Mathematical) necessary conditions for the selection of gradient vectors in DTI, *J Magn Reson* 172 (2005), 238–241.
- A. Özcan, A new model for diffusion weighted MRI: Complete fourier direct MRI, *Conf Proc IEEE Eng Med Biol Soc* 2010 (2010c), 2710–2713.
- A. Özcan, Characterization of imaging gradients in diffusion tensor imaging, *J Magn Reson* 207 (2010a), 24–33.
- A. Özcan, Comparison of the complete fourier direct MRI with existing diffusion weighted MRI methods, *IEEE International Symposium on Biomedical Imaging: From Nano to Macro* (2011), 931–934.
- A. Özcan, Minimization of imaging gradient effects in diffusion tensor imaging, *IEEE Trans Medical Imaging* 30 (2011), 642–654.
- A. Özcan, Noise and nonlinear estimation with optimal schemes in DTI, *Magn Reson Imaging* 28 (2010b), 1335–1343.
- A. Özcan, J.D. Quirk, Y. Wang, Q. Wang, P. Sun, W.M. Spees, and S.-K. Song, The validation of complete fourier direct MR method for diffusion MRI via biological and numerical phantoms, *Proceedings of the 33rd Annual International Conference of the IEEE EMB Society, Boston, MA* (2011), 3756–3759.
- S. Pajevic and C. Pierpaoli, Color schemes to represent the orientation of anisotropic tissues from diffusion tensor data: Application to white matter fiber tract mapping in the human brain, *Magn Reson Med* 42 (1999), 526–540.
- N.G. Papadakis, D. Xing, C.L. Huang, L.D. Hall, and T.A. Carpenter, A comparative study of acquisition schemes for diffusion tensor imaging using MRI, *J Magn Reson* 137 (1999), 67–82.
- A.B.N. Shiryaev, *Probability*, Springer, New York, 1996.
- S.K. Song, Z. Qu, E.M. Garabedian, J.I. Gordon, J. Milbrandt, and J.J. Ackerman, Improved magnetic resonance imaging detection of prostate cancer in a transgenic mouse model, *Cancer Res* 62 (2002), 1555–1558.
- E.O. Stejskal and J.E. Tanner, Spin diffusion measurements: Spin echoes in the presence of a time-dependent field, *J Chem Phys* 42 (1965), 288–292.
- H.C. Torrey, Bloch equations with diffusion terms, *Phys Rev* 104 (1956), 563–565.
- J.D. Tournier, F. Calamante, D.G. Gadian, and A. Connelly, Direct estimation of the fiber orientation density function from diffusion-weighted MRI data using spherical deconvolution, *Neuroimage* 23 (2004), 1176–1185.
- D.S. Tuch, T.G. Reese, M.R. Wiegell, and V.J. Wedeen, Diffusion MRI of complex neural architecture, *Neuron* 40 (2003), 885–895.
- S.K. Warfield, F. Talos, C. Kemper, E. Cosman, A. Tei, M. Ferrant, B.M.M. Macq, W.M. Wells III, P.M. Black, F.A. Jolesz, and R. Kikinis, Augmenting intraoperative MRI with preoperative FMRI and DTI by biomechanical simulation of brain deformation, *Proceedings of SPIE, San Diego, CA*, 2003, pp. 77–86.
- V.J. Wedeen, P. Hagmann, W.Y. Tseng, T.G. Reese, and R.M. Weisskoff, Mapping complex tissue architecture with diffusion spectrum magnetic resonance imaging, *Magn Reson Med* 54 (2005), 1377–1386.
- J. Xu, P.A. Humphrey, A.S. Kibel, A.Z. Snyder, V.R. Narra, J.J. Ackerman and S.K. Song, Magnetic resonance diffusion characteristics of histologically defined prostate cancer in humans, *Magn Reson Med* 61 (2009), 842–850.

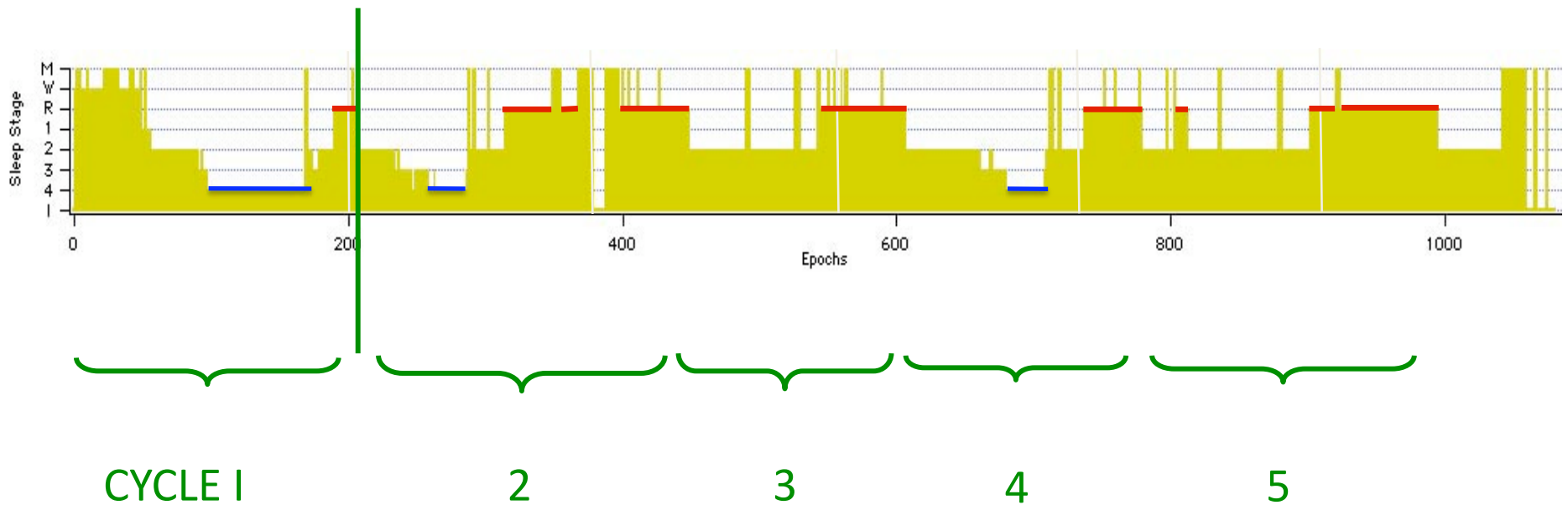
Appendix 4
Importance of Sleep to Humans

WHAT HAPPENS TO THE BRAIN WHEN WE SLEEP?

Brain electrical activity changes in a highly stereotypic pattern

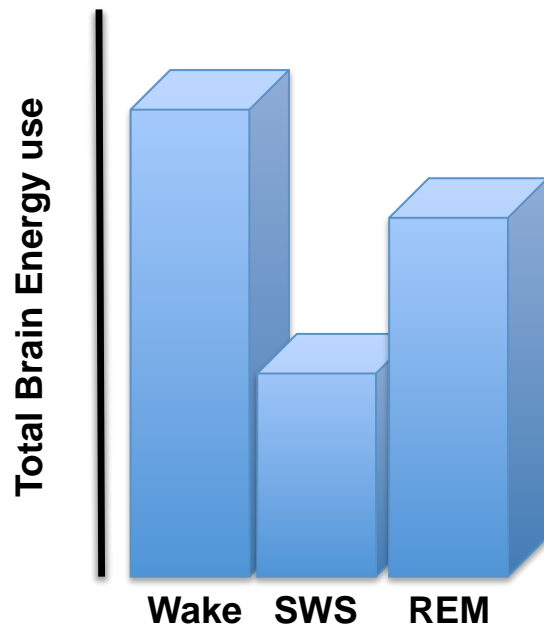


That occurs cyclically through the night (2-7 cycles/night)



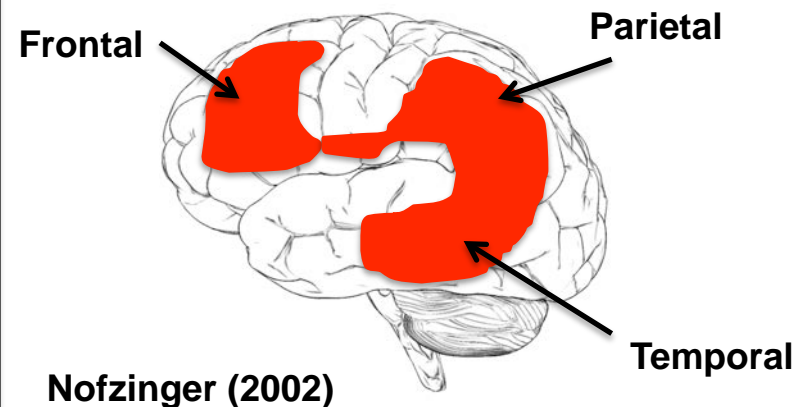
WHAT HAPPENS TO THE BRAIN WHEN WE SLEEP?

The brain reduces its energy use in deep sleep

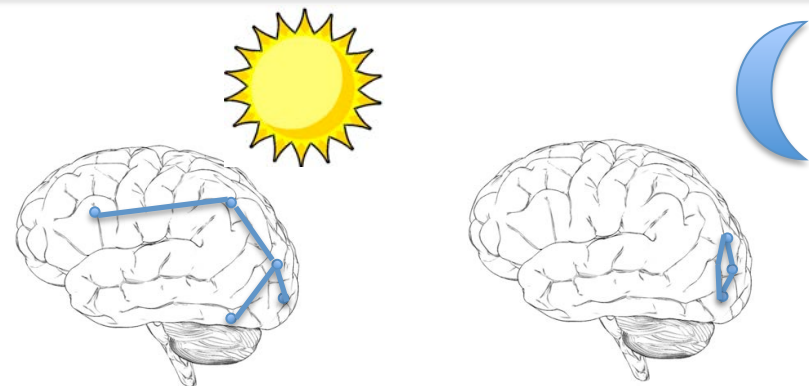


Maquet (1995), Braun et al. (1997)

This reduced energy consumption is greatest in parts of the brain involved in attention, cognition and integration of information



The transfer of information between brain regions – the functional connections between brain networks – becomes less global and more local (Horowitz et al., 2009; Spoormaker et al., 2010; Larson-Prior et al., 2009, 2011)

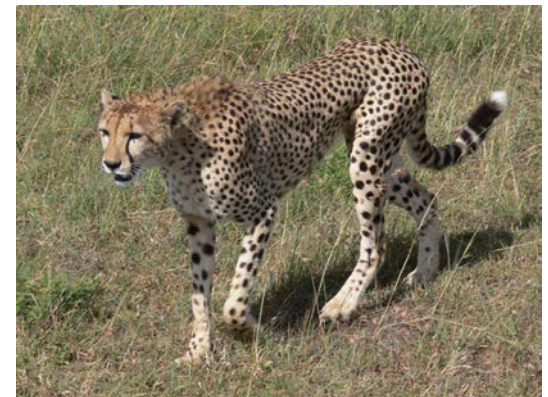


WHY DO WE SLEEP?

We do not know WHY we sleep, but we know that it is important, because

All organisms sleep:

Even if it is life threatening!



WHY DO WE SLEEP?

And when we don't sleep:

Hours sleep/night

Daytime effect

Possible long-term consequences

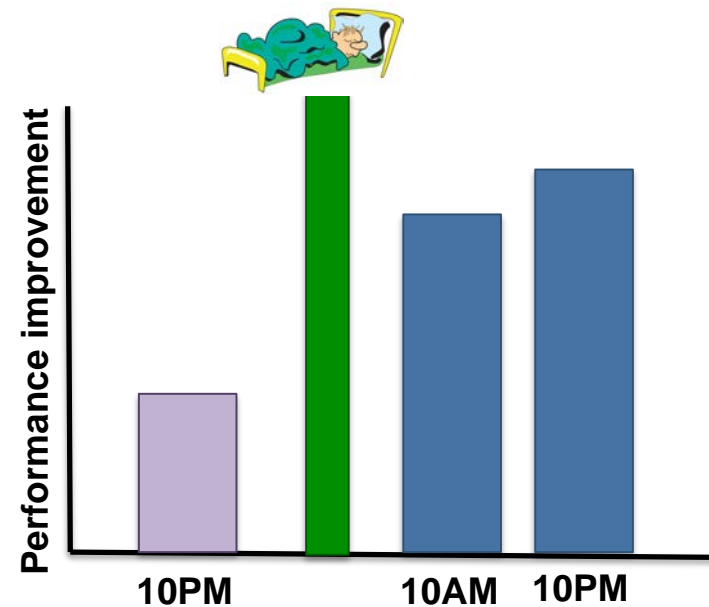
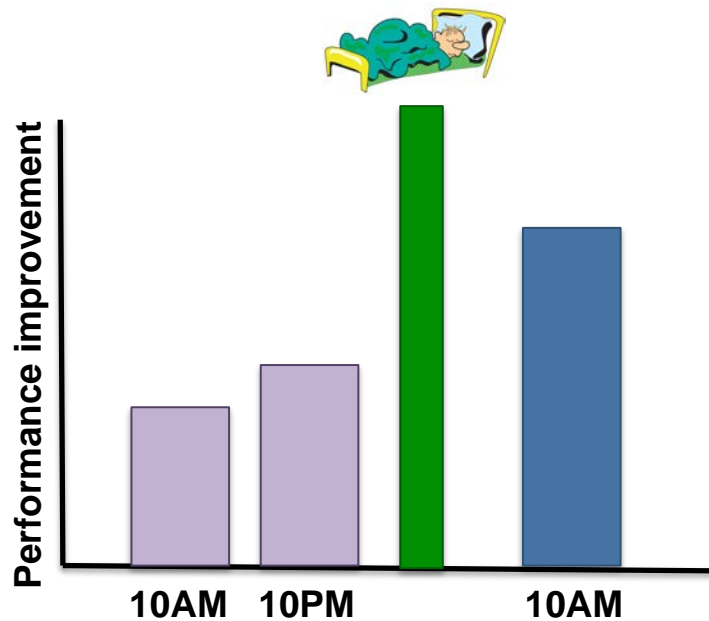


WHAT ARE THE BENEFITS OF SLEEP?

Sleep promotes at least some types of learning and memory



Sleep improves memory of a learned sequence of finger taps to a greater extent than is seen with the passage of time alone

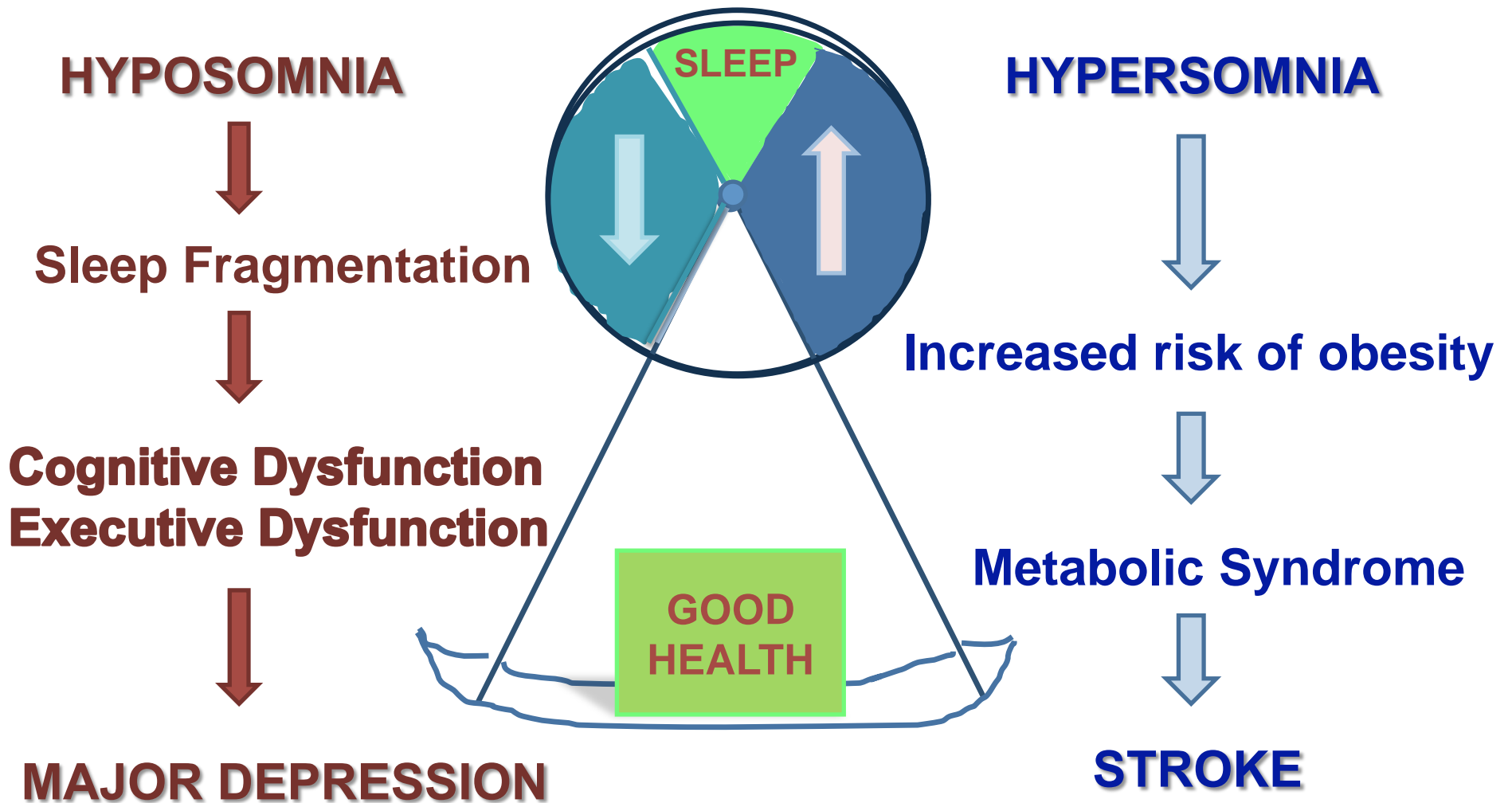


Walker and Stickgold (2006) Ann Rev Psychology 57:139

 No sleep, day 1  After sleep, day 2

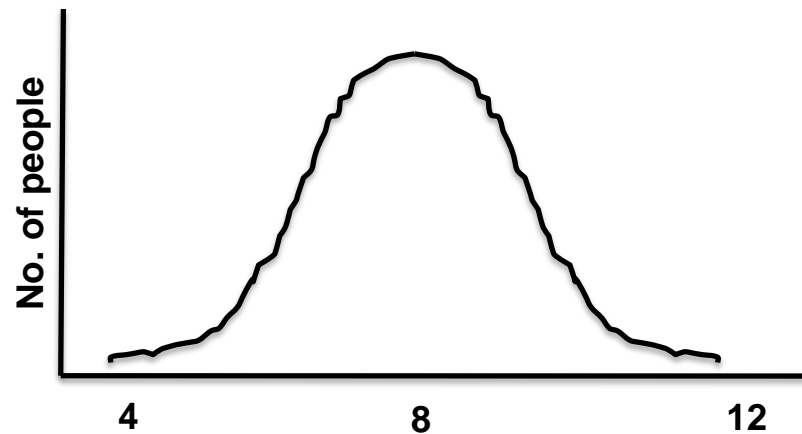
WHAT ARE THE BENEFITS OF SLEEP?

Sleep promotes good mental and physical health



HOW MUCH SLEEP DO WE NEED?

Humans sleep between 4 and 10 hours/night – there is no number of hours that is “right” for everyone



The amount of time we need to sleep changes with age

How Much Sleep Do You Really Need?	
Age	Sleep Needs
Newborns (0-2 months)	12-18 hours
Infants (3 to 11 months)	14 to 15 hours
Toddlers (1-3 years)	12 to 14 hours
Preschoolers (3-5 years)	11 to 13 hours
School-age children (5-10 years)	10 to 11 hours
Teens (10-17)	8.5-9.25 hours
Adults	7-9 hours

Source: National Sleep Foundation